CONFIDENTIAL

College Note No. 31

THE COLLEGE OF AERONAUTICS

CRANFIELD

EXPERIMENTAL INVESTIGATION OF THE INTERFERENCE OF A BODY ON A LOW ASPECT RATIO WING OF RECTANGULAR PLANFORM AT A MACH NUMBER OF 2

by

J.R. BUSING, G.B. MARSON and G.M. LILLEY

NOTE NO. 31

JUNE, 1955.

THE COLLEGE OF AERONAUTICS

CRANFIELD

An Experimental Investigation of the Interference of a Body on a Low Aspect Ratio Wing of Rectangular Planform at a Mach Number of 2

-by-

J.R. Busing,* B.E., B.Sc., D.C.Ae.,

G.B. Marson, B.Sc.,

G.M. Lilley, M.Sc., D.I.C.,
A.F.R.Ae.S., A.M.I.Mech.E.

of the Department of Aerodynamics

SUMMARY

Results are given of pressure measurements on a wing of gross aspect ratio approximately 2/3 mounted on a cylindrical body with an ogival nose, made at a Mach number of 2.00 in the 9in. x 9in. supersonic wind tunnel at the College of Aeronautics. The wing section was a single wedge having a 6° total nose angle. The ranges of body incidence and roll in these tests were from 0° to 30°, and 0°, 30°, 60° and 90° respectively. The normal force, lift, drag and side force coefficients, and rolling and pitching moments were obtained from the pressure measurements.

/The pressure ...

MEP

* Seconded from the Aerodynamics Section of the Navigational Project Division, English Electric.

The pressure distributions for small angles of incidence have been compared with a modified form of Morikawa's approximate solution for a semi-infinite wing mounted on an infinitely long cylindrical body. Fair agreement was obtained at all roll angles, between this theory and experiment, except in the region of influence of each tip vortex, and far downstream of the leading edge. A detailed comparison with the theories of Nielsen and others was not made due to the lack of appropriate numerical data. It was noted however that the effect of the body could crudely be represented by replacing it by a plane reflection plate at the wing root.

At higher angles of incidence the non-linear effects on the pressure distribution are large, but are of opposite sign on the upper and lower surfaces. Thus the integrated results for normal force are almost linear with incidence. The remaining non-linear effects on normal force and centre of pressure can be explained in terms of the viscous cross flow over a wing of small aspect ratio. When the viscous effects are included the measured normal force agrees fairly well with that predicted by the empirical relation of Nielsen and Kaattari. The measured chordwise centre of pressure at 0° roll moved downstream from about 0.25 to 0.45 chord as the incidence was increased from 0° to 30°. Similar results were obtained for 30° and 60° roll. The measured spanwise centre of pressure at 0° roll for each half wing moved outboard from about 0.60 to 0.65 of the semi-span as the incidence increased to 10°, and then remained approximately fixed up to 30° incidence. At larger roll angles the outboard movement continued over a greater range of incidence. It was found from the spanwise pressure distributions and the integrated values of rolling moments that the sign and approximate magnitude of the rolling moment could be obtained from the lower surface pressures on the downgoing wing. This was due to the separation of flow on the upper surface of the downgoing wing and the separation on both surfaces of the upgoing wing as a result of the influence of the body on the spanwise flow on both wings. The rolling moment was zero at 0° and 90° roll and reached a maximum at about 60° roll.

/1. ...

1. List of Contents

Figures

1. Dimensions of model and positions of pressure tappings
2. Orientation of model in tunnel
3. Position of Mach waves on wing
4. Theoretical pressure distribution on wing
5. Chordwise pressure distribution on wing at 0° roll, y/a = 2.49
6. " " " " " " " y/a = 2.15
7. " " " " " " " y/a = 1.94
8. " " " " " " " y/a = 1.625
9. " " " " " " " y/a = 1.43
10. " " " " " " " y/a = 1.09
11. Spanwise pressure distribution on wing at 0° roll
12. Chordwise distribution of normal force at 0° roll y/a = 2.49
13. " " " " " " " y/a = 2.15
14. " " " " " " " y/a = 1.94
15. " " " " " " " y/a = 1.625
16. " " " " " " " y/a = 1.43
17. " " " " " " " y/a = 1.09
18. Chordwise pressure distribution on wings at 30° roll y/a = 2.49
19. " " " " " " " y/a = 2.15
20. " " " " " " " y/a = 1.94
21. " " " " " " " y/a = 1.625
22. " " " " " " " y/a = 1.43
23. " " " " " " " y/a = 1.09
24. Spanwise pressure distribution on wings at 30° roll
25. Chordwise distribution of normal force at 30° roll y/a = 2.49
26. " " " " " " " y/a = 2.15
27. " " " " " " " y/a = 1.94
28. " " " " " " " y/a = 1.625
29. " " " " " " " y/a = 1.43
30. " " " " " " " y/a = 1.09

Figures, (Contd.)

31. Chordwise pressure distribution on wings at 60° roll, y/a = 2.49
32. " " " " " " " y/a = 2.15
33. " " " " " " " y/a = 1.94
34. " " " " " " " y/a = 1.625
35. " " " " " " " y/a = 1.43
36. " " " " " " " y/a = 1.09
37. Spanwise pressure distribution on wings at 60° roll,
38. Chordwise distribution of normal force at 60° roll, y/a = 2.49
39. " " " " " " " y/a = 2.15
40. " " " " " " " y/a = 1.94
41. " " " " " " " y/a = 1.625
42. " " " " " " " y/a = 1.43
43. " " " " " " " y/a = 1.09
44. Comparison of pressure distr. with theory for wing alone, $\alpha = 5^{\circ}$ y/a = 2.49
45. " " " " " " y/a = 2.15
46. High incidence chordwise pressure distribution at 0° roll, y/a = 2.49
47. " " " " " " y/a = 2.15
48. " " " " " " y/a = 1.94
49. " " " " " " y/a = 1.625
50. " " " " " " y/a = 1.43
51. " " " " " " y/a = 1.09
52. " " spanwise " " "
53. " " chordwise " " "
30° roll, y/a = 2.49
54. " " " " " " y/a = 2.15
55. " " " " " " y/a = 1.94
56. " " " " " " y/a = 1.625
57. " " " " " " y/a = 1.43
58. " " " " " " y/a = 1.09
59. " " spanwise " " "
60. " " chordwise " " "
60° roll, y/a = 2.49

/61. ...

Figures, (Contd.)

61. High incidence chordwise pressure distribution at 60° roll, y/a = 2.15
62. " " " " " y/a = 1.94
63. " " " " " y/a = 1.625
64. " " " " " y/a = 1.43
65. " " " " " y/a = 1.09
66. " " spanwise " "
67. " " chordwise " "
at 90° roll, y/a = 2.49
68. " " " " " y/a = 2.15
69. " " " " " y/a = 1.94
70. " " " " " y/a = 1.625
71. " " " " " y/a = 1.43
72. " " " " " y/a = 1.09
73. " " spanwise " "
74. Variation of normal force coefficient with pitch angle
75. Comparison of normal force coefficients at zero roll with theory
76. Movement of centre of pressure with pitch angle at various roll angles
77. " " " " " " " " " 30° roll
78. " " " " " " " " " 60° roll
79. Variation of lift coefficient with incidence
80. Variation of drag coefficient with incidence
81. Variation of side force coefficient with sideslip angle
82. Variation of pitching moment coefficient with incidence
83. Variation of rolling moment with angle of roll
84. Variation of rolling moment with angle of sideslip
85. Spanwise distribution of normal force coefficients
86. Chordwise pressure distribution in wing-root body junction.

2. List of Symbols

A aspect ratio

a body radius

B $\sqrt{M^2 - 1}$

c wing chord length

C_D drag coefficient $= C_N \sin \alpha \cos \beta$

C_L lift coefficient $= C_N \cos \alpha$

C_l rolling moment coefficient $= \dfrac{\text{R.M.}}{\frac{1}{2}\rho_o u_o^2 S_w s}$

$C_{m_{1/4}}$ pitching moment coefficient about 1/4 chord point $= \dfrac{\text{P.M.}_{1/4}}{\frac{1}{2}\rho_o u_o^2 S_w . c}$

C_N total normal force coefficient

$$= \frac{N}{\frac{1}{2}\rho_o u_o^2 S_w} = \frac{s}{s-a} \int_{a/s}^{1} C_n d\left(\frac{y}{s}\right) .$$

C_n local normal force coefficient for a column

$$= \int_o^1 \Delta C_p d\left(\frac{x}{c}\right) .$$

C_p pressure coefficient $= \dfrac{p - p_o}{\frac{1}{2}\rho_o u_o^2}$

ΔC_p local normal force coefficient at a point

$= \left[(C_p \text{ on lower surface}) - (C_p \text{ on upper surface})\right] \delta .$

C_Y side force coefficient $= C_N \sin \alpha \sin \beta .$

F $\dfrac{2}{\pi}\left[1 + \dfrac{1}{(y+\eta)^2}\right] \dfrac{1}{\sqrt{\lambda^2 - \eta^2}}$

G Green's function

h local chordwise position of centre of pressure for a column

$\bar{h}$ chordwise position of resultant centre of pressure

L lift

l length

List of Symbols (Contd.)

M	free stream Mach number
N	Normal force
$P.M._{1/4}$	pitching moment about 1/4-chord point
p	surface static pressure
p_o	freestream static pressure
$R.M.$	rolling moment
r	radius in polar-co-ordinates
S_w	net wing area
s	wing semi-span (gross)
$\bar{s}$	spanwise position of centre of pressure
t	time
u_o	freestream velocity
x	chordwise co-ordinate on model
y	spanwise co-ordinate on model
α	angle of incidence
β	angle of sideslip
δ	wing wedge semi-angle
θ	angle of pitch, polar co-ordinate angle
ρ_o	free stream density
ϕ	angle of roll, velocity potential
λ	$\frac{x-x_o}{Ba}$
η	$\frac{B(y_o-y)}{Ba}$

3. Introduction

This report presents the results of part of an investigation into the interference between a body and wing of low aspect ratio at supersonic speeds. The results of the initial study, by flow visualisation techniques, have been reported separately in ref. 1.

The present state of knowledge on the problem of wing body interference at supersonic speeds has been reviewed recently by Lawrence and Flax[2]. At small angles of incidence linearised theory provides a basis on which calculations can be made. However, when the aspect ratio is small, the interference effects are too complex for any accurate theoretical predictions to be made. In addition, except at small angles of incidence, viscous effects, detached shock waves, etc., render the problem at present incapable of solution. Recourse to experiment is therefore essential before any adequate theory can be formulated. The present tests deal with one particular wing-body combination in which a low aspect ratio wing of single wedge section is mounted on a cylindrical body with a tangent ogival nose.

Several methods, based on linearised theory have been proposed for calculating wing-body effects at supersonic speeds. In these methods the problem can be subdivided as follows.-

(a) body alone at incidence
(b) body at zero incidence - wing at incidence
(c) wing at incidence in the presence of the body alone upwash field.

The methods for the calculations of the pressure distribution over bodies of revolution at incidence are described by Lawrence and Flax[2]. The calculation of the pressure distribution on a rectangular wing of small aspect ratio has been given by Gunn[3].

The interference problem is simplified if the wing is mounted far downstream of the nose of a body of circular cross-section. In this case the body upwash field can be taken as that for an infinite circular cylinder[4]. If the wing has no sweepback and is of infinite span then the effect on the wing of the upwash field due to the body, outside the influence of the root Mach cone, is that calculated by Kirkby and Robinson[5]. The modifications to allow for sweepback (supersonic leading edges) and finite span have been considered by Bolton-Shaw[6].

For wings of infinite aspect ratio mounted on bodies of finite length, the method of Ferrari[7] is available. On the other hand, Morikawa[8] and Nielsen[9] have tackled the particular case of a semi-infinite rectangular wing mounted on an infinite cylindrical body of circular cross-section at incidence.

Although Morikawa's method is exact a complete solution is not yet available and the present numerical results for the pressure distribution on the wings are only approximate. Nielsen's method has a wider application, but even here complete numerical results are not available. Bolton-Shaw has also proposed a method for dealing with these cases although no numerical results have been given. A further account, dealing with wings of large aspect ratio mounted on bodies of arbitrary shape and circular cross-section, has been given by Chester[10]. When the wing-body combination is slender, the results of Ward[11], Browne, Friedman and Hodes[12] are available. Empirical relations for the interference of a body on a wing have been formulated by Nielsen and Kaattari from an examination of a large number of experimental results on various wing-body combinations.[13]

In view of the lack of appropriate numerical results from the above theoretical methods, especially for wings of small aspect ratio having rectangular planforms, it has only been possible to compare the present experimental results with those of Morikawa, in which a modification for the effect of the tip has been included. Since this method deals with a flat plate wing, only the effects of incidence and not of wing thickness are compared with theory.

A further discussion on the linearised supersonic theory of wing-body interference is given in Appendix 1. The pressure distribution on the wing in the presence of the body upwash is discussed in Appendix 2.

4. Experimental Details

The work was performed in the 9in x 9in supersonic wind tunnel at the College of Aeronautics, a full description of which is given in ref. 1. The tunnel was fitted with a fixed wooden liner giving a Mach number along the working section of 2.00 ± 0.01.

The model, which is described in the next section, was supported through a vernier coupling on a vertical crescent. The model incidence could be remotely controlled between $+30^{\circ}$ and -5° to an accuracy of $\pm$ 1 minute, and the roll could be adjusted in the tunnel to the same degree of accuracy by means of the vernier coupling. The tunnel stagnation pressure was automatically controlled to 20in. Hg within 0.02in Hg, and the stagnation temperature was maintained at 26°C + or - 1°C. Due to the limited size of the silica gel drying plant it was never possible to reduce the moisture content of the tunnel air to less than one part in 2000.

Pressure tappings on one wing of the model were connected through a pneumatic clamp to a multi-tube vertical mercury manometer. The tubes were clamped while pressure readings were taken. It was found necessary to wait for three minutes after changing the incidence setting before clamping the tubes in order to ensure that the recorded pressures on the manometer had reached steady state values.

Seventeen holes, forming a chordwise column, could be pressure plotted simultaneously and a set of readings was taken at incidences of 0°, $2\frac{1}{2}^\circ$, 5°, $7\frac{1}{2}^\circ$, 10°, $12\frac{1}{2}^\circ$, 15°, $17\frac{1}{2}^\circ$, 20° 25° and 30° during each run. Each set of measurements was repeated on six such columns for all roll angles at intervals of 30°. Since the pressure holes were drilled in one surface of one half-wing only, the complete pressure distribution on the whole wing at an angle of roll ϕ was obtained from measurements at angles of roll ϕ, $180^\circ - \phi$, $180 + \phi$, and $360^\circ - \phi$.

As described in the next section, nine additional pressure holes were made to enable pressures to be measured closer to the leading edge.

The complete model was tested at a Reynolds number of 2.5×10^6 per foot. The pressure distributions were plotted to a large scale and integrated to find the area and first moment using a 'Stanley' integrator.

5. Description of the Model

Fig. 1 shows a plan view of the model, indicating its main dimensions. The cylindrical body is 0.735in. diameter and has a tangent ogival head of length 2.18in., with a nose semi-angle of 20°. The wings are of rectangular planform with a gross aspect ratio of 0.664 and net aspect ratio 0.422. They have a 6° single-wedge section and are symmetrically placed with respect to the body centre line. The wing leading edge is positioned 5.45in. from the body nose, and has a radius of 0.001in. The body is made in two parts, to enable pressure tubes from the wing to be connected and led away to the rear of the sting. Seventeen holes were drilled in a spanwise direction through one wing. Six 0.018in. diameter holes were drilled through the upper surface into each of these spanwise holes giving six columns of seventeen holes each. For each test, the holes on five columns were filled with plasticine, the remaining seventeen holes being connected through tubing to the manometers. After all pressure measurements had been made with these tappings, three small tubes of 1mm. outside diameter were soldered to the undersurface of the wing. This allowed nine pressure tappings to be made near the leading edge, where the wing was too thin for spanwise holes to be drilled. The positions of the holes are shown diagrammatically

in fig. 1, and their exact co-ordinates are given in table I.

The wing tip and base were not pressure plotted in these tests.

6. Reduction and Presentation of Data

6.1 Definition of orientation

In order to describe the orientation of the model, we may define sets of wind, (X',Y',Z') and body, (X,Y,Z) axes as shown in fig. 2. The wind X'-axis coincides with the upstream direction. The body axes coincide with the wind axes at zero pitch θ, and roll, ϕ. In these tests the model attitude is defined in terms of an initial pitch θ about the wind X'-axis and then a roll ϕ about the body X-axis. The model attitude may also be expressed in terms of the angle of incidence, α, and the angle of sideslip, β.*

where, as shown in fig. 2, $\tan \alpha = \tan \theta \cos \phi$
$\sin \beta = \sin \theta \sin \phi$.

6.2 Reduction of the pressure measurements

All pressures were reduced to the coefficient form

$$C_p = \frac{p - p_o}{\frac{1}{2} \rho_o u_o^2}$$

where p_o, ρ_o and u_o are the freestream pressure, density and velocity respectively. Owing to the difficulties of drilling the pressure holes, forming the columns, some of these were scattered slightly about a mean line, but for purposes of plotting the results, mean chordwise and spanwise positions of the holes were taken.

The experimental pressure distributions for values of incidence below 10° have been plotted in terms of $B(C_p - C_{p_o})/\alpha$ (where $B = \sqrt{M^2-1}$, C_{p_o} is the value of C_p at $\alpha = 0$, and α is the incidence) in order to facilitate comparison with linearised theory. The pressure distributions for higher incidences have been plotted in terms of C_p. In each case, chordwise distributions have been given for each column, and also spanwise distributions at a number of chordwise stations. The nine pressure tappings near the leading edge were positioned approximately at regular intervals in the spanwise direction.

* This corresponds to the tangent definition for incidence and the sine definition for sideslip as described by Warren (ref. 16).

The pressures obtained from these holes have been interpolated to give additional values, at the positions of the six main columns.

The local loading (or local normal force coefficient) ΔC_p is defined as

$$\Delta C_p = (C_{p_L} - C_{p_U}) \cos \delta$$

where δ denotes the wing half nose angle and suffixes L and U refer to lower and upper surfaces respectively. The local loading distribution on each column was integrated for each incidence and roll angle to give the local chordwise loading C_n, and the local chordwise centre of pressure, distance h from the leading edge. These values of C_n were then plotted against spanwise position, and integrated to give the total normal force and centre of pressure for the half-wing.

The above quantities, in coefficient form, are defined as follows

Local chordwise loading coefficient

$$C_n = \int_o^1 \Delta C_p \, d\left(\frac{x}{c}\right)$$

Local chordwise position of the centre of pressure measured from the leading edge as a fraction of the wing chord

$$h\left(\frac{y}{s}\right) = \frac{\int_o^1 \frac{x}{c} \Delta C_p \, d\left(\frac{x}{c}\right)}{\int_o^1 \Delta C_p \, d\left(\frac{x}{c}\right)}$$

Normal force coefficient for net half-wing

$$C_N = \frac{s}{s - a} \int_{a/s}^1 C_n \, d\left(\frac{y}{s}\right)$$

Spanwise position of the centre of pressure for net half-wing, as a fraction of the gross semi-span

$$\bar{s} = \frac{\int_{a/s}^1 C_n \frac{y}{s} \, d\left(\frac{y}{s}\right)}{\int_{a/s}^1 C_n \, d\left(\frac{y}{s}\right)}$$

Chordwise position of the centre of pressure for the net half-wing as a fraction of the wing chord

$$\bar{h} = \frac{\frac{s}{s-a}\int_{a/s}^{1} C_n h \, d\frac{y}{s}}{C_N}$$

where c = wing chord
s = gross semi span
a = body radius.

6.3 Resolution and definition of forces and moments

From the pressure plotting results the total normal force, N, perpendicular to the plane of the wings has been obtained. The resolutes lift, drag,* and side force in terms of their non-dimensional coefficients are defined as follows.-

lift coefficient	$C_L = C_N \cos \alpha$
drag coefficient	$C_D = C_N \sin \alpha \cos \beta$
side force coefficient	$C_Y = C_N \sin \alpha \sin \beta$

where $C_N = \frac{N}{\frac{1}{2}\rho_o u_o^2 S_w}$ and S_w is the net wing area.

The rolling and pitching moments with respect to body axes have been calculated for the two half-wings in combination, from the loading distributions on each wing. Their values are given by

Rolling moment coefficient about body centre line $C_l = \frac{R.M.}{\frac{1}{2}\rho_o u_o^2 S_w . s}$

Pitching moment coefficient about 1/4-chord locus $C_{m_{1/4}} = \frac{P.M.}{\frac{1}{2}\rho_o u_o^2 S_w . c}$

It will be seen that all the above coefficients are defined in terms of the net wing area.

---

* This excludes the skin friction drag.

6.4 Accuracy of the results

The mercury manometers could be read to an accuracy of ± 0.02in. giving an accuracy in C_p of approximately ± 0.003. A number of repeat measurements taken at different times during the programme showed a repeatability in C_p of ± 0.01.

Since the pressures on the upper and lower surfaces of the wing have been measured with the wing in different positions in the tunnel working section, small errors have arisen due to variations in pitch and yaw across the working section. Corrections to the readings have been applied, where these are significant, and the values of C_p corresponding to zero incidence have been found by interpolation. (It will be found, however, that due to the method of correcting the results slight discrepancies occur between the plotted values of ΔC_p and those found from the $C_p - C_{p_o}$ curves.)

In view of the small errors in pitch and yaw in the working section it is estimated that the errors in quoted values of incidence and yaw should be within ± 0.1°.

The accuracy of the values obtained for force and moment coefficients depended to a large extent on the accuracy in plotting and use of the integrator. Careful checks showed that the values of the coefficients were repeatable to within ± 0.01 except for the rolling moment which was within ± 0.02. The positions of centre of pressure, expressed non-dimensionally were repeatable to within ± 0.01.

6.5 Presentation of the more important results

The pressure results for angles of incidence below 10° are given as chordwise distributions of $B\Delta C_p/a$, and chordwise and spanwise distributions of $B(C_p - C_{p_o})/a$ in figs. 5 to 43. The pressure results for the higher incidences are plotted as chordwise and spanwise distributions of C_p in figs. 46-73. These graphs include results for 90° roll angle.

The remaining figures show the values of the forces and moments derived from the pressure measurements as described in 6.3. Figure 74 shows the variation of normal force coefficient with incidence for each half-wing, at various roll angles, while in fig. 75, the results for 0° roll only, are compared with some theoretical predictions. Figs. 76-78 show the movement of the centre of pressure with incidence for various roll angles. These are followed by the lift, drag and side-force results, plotted against incidence for the two half-wings in combination, in figs. 79, 80 and 81. Fig. 82 shows the

variation of the pitching moment coefficient with incidence, and figure 83 the variation of side force coefficient with sideslip angle. The rolling moment coefficient is plotted against angle of roll, for various angles of pitch, in fig. 83 and against angle of sideslip, for various incidences, in fig. 84. Finally fig. 85 shows the spanwise distribution of the local normal force coefficients for each column of pressure tappings, at various incidences up to 30°, and roll angles of 0°, 30° and 60°.

7. Theoretical results

As stated in the introduction, the experimental pressure distributions have only been compared with the approximate results obtained from Morikawa's theory[8], to which a modification has been made to account for the effects of the tip. The method of calculating this correction is given in Appendix 2.

For purposes of calculation, the wing may be divided into a number of distinct regions by Mach waves from various points at the extremities of the wing, and their reflections. These are shown in fig. 3. Fig. 4 shows the theoretical pressure distribution on the wing surface of the wing body combination, as given by the modified form of Morikawa's theory.

At the leading edge, the pressure coefficients are equal to those of a wing in an upwash field due to an infinite cylindrical body, given by $\bar{\alpha} = \alpha(1 + a^2/y^2)$ where $\alpha\, a^2/y^2$ is the apparent incidence of the wing due to upwash, and α is the common body-wing incidence. Thus the pressure coefficients at the leading edge decrease in a spanwise direction (from the value of $BC_p/\alpha = 4.0$ at the wing root). In region I (fig. 3) the 'twisted wing' effect, due to the upwash distribution, causes the pressure coefficients in this region to increase slightly in the chordwise direction. Otherwise, the spanwise distribution is similar to that at the leading edge.

In region II, behind the Mach wave from the leading edge tip, the pressure coefficients are obtained by subtracting the tip correction from the solution used in region I. In region III, there is no influence due to the tip, and thus Morikawa's solution can be used unmodified. It will be seen that the effect of the wing-body interference in this region is to cause the pressure coefficients to fall off gradually downstream of the root Mach line. The pressure coefficients in region IV are obtained by subtracting the tip correction from Morikawa's solution.

Theoretically the disturbance from the opposite wing root should propagate round the body on a constant angle helix and reach the wing root at $x/Ba = \pi$. In the approximate results deduced from Morikawa's theory this disturbance reaches the wing root at $x/Ba = 2$. Thus no theoretical values for the pressure coefficients have been calculated near the root, beyond $x/Ba = 2$ (see Appendix 1 and fig. 86). In addition, for this model configuration, the disturbance from the tip strikes the wing-body junction at $x/Ba = 1.72$. Since the magnitude of the reflected wave has not been calculated, this is a further reason why no theoretical values are given beyond Region IV.

It should be noted that the theoretical values given above are for a flat plate wing. Corrections can easily be calculated for the finite wing thickness in the region in front of the root Mach cone. Over the rest of the wing surface, the thickness correction, for a single wedge aerofoil section, could be obtained from either Chester,[10] or Nielsen's theory[9], but by the method of presentation of the experimental data, the thickness effects have been eliminated.

In the diagrams showing the pressure distributions, the leading edge values are plotted from shock-expansion theory allowing for the body upwash. It should be noted that these results do not correspond with those given by linearised theory, and are not linear with incidence.

It can be shown by linearised theory that the values of lift, drag and moment coefficients for a flat plate wing alone having the same aspect ratio as the gross aspect ratio of the wing body combination, are

$$C_L = \frac{4a}{B}\left(1 - \frac{1}{2BA}\right)$$

$$C_D = \frac{4a^2}{B}\left(1 - \frac{1}{2BA}\right)$$

$$C_{m_{1/4}} = -\frac{4a}{B}\left(\frac{1}{4} - \frac{5}{24AB}\right)$$

and the distance of the centre of pressure from the leading edge is $\left(\frac{3AB - 2}{6AB - 3}\right)$

where a = wing incidence,

$B = \sqrt{M^2 - 1}$

A = wing aspect ratio.

The value of normal force coefficient C_N for a wing having an aspect ratio equal to the net aspect ratio A', can be obtained by integration from the results given in ref. 3, i.e. for $A' = 0.422$ and $M = 2.0$, $C_N = 0.80\ a$, and the position of the centre of pressure is at a chordwise distance of $0.25c$ from the leading edge and 0.624 of the semi-span from the centre line.

The empirical relation quoted by Nielsen and Kaattari[13] for the normal force on the wing due to the presence of the body gives for this wing-body combination a value equal to 1.38 times the normal force on the wing alone based on the exposed wing area.

The result obtained from slender body theory for the lift L_w on the wing in the presence of the body is

$$L_w = \left(1 + \frac{a}{s}\right) L'_w$$

where L'_w is the lift on the wing alone (based on the exposed area). For this wing body combination $(1 + a/s) = 1.368$. Thus the factor due to interference differs only slightly from that suggested by Nielsen and Kaattari.

It should be noted that the aspect ratio, based on exposed, or net, wing area in these experiments is 0.422 and is therefore in the range where the non-linear viscous effects on the lift are important. The total normal force coefficient on a wing of very small aspect ratio in viscous incompressible flow, given by the empirical formula of Flax and Lawrence[14] is

$$C_N = \frac{\pi}{2} A\, a + k a^2$$

where k is obtained empirically and is approximately equal to 2. A similar relation given by Cheng is

$$C_N = \frac{\pi}{2} A a + \pi\, (2A)^{1/3}\, a^{5/3},$$

but this relation does not agree with existing low speed experimental data when A is greater than about 0.1.

It has been assumed in comparing the present experimental data with the above theoretical and empirical results that the viscous (non-linear) term in C_N is not affected by the body interference. This is not meant to imply that such body interference does not exist but rather that the effect is considerably less than the body interference on the

linear terms. Physically, this can be justified by the crude argument that the non-linear viscous effects are more related to the flow near the wing tips, where the body interference is small, whereas the linear wing effects are more related to the flow near the wing body juction where the body interference is large.

Similarly the pitching moment coefficient and the movement of the wing centre of pressure due to these viscous effects can be calculated in terms of the crossflow coefficient k in the expression for C_N above.

8. Discussion of the experimental results

8.1 Results at low incidence

(i) Roll angle $\phi = 0$

(a) The chordwise pressure distributions obtained from experiment show good agreement with the theoretical values except near the tip and far downstream from the leading edge. (Figs. 5 to 10). Downstream of the leading edge, near the tip, (fig. 5) the pressure coefficients are underestimated slightly by the modified Morikawa theory over the forward part of the lower surface. On the upper surface, large suctions occur along the whole of the wing tip at incidences above 2°. This high suction is due to separation of the flow into the tip vortex, which begins to form almost immediately behind the leading edge. This is evident in the pressure distributions as a large non-linear variation of suction with incidence.

Near the leading edge the measured pressures on the outboard columns (figs. 5 and 6) agree reasonably well with shock expansion theory, but nearer the root (figs. 9 and 10) the leading edge pressure coefficients given by this theory are too high, at incidences above 5°. It is suggested that this is due to a detached shock wave caused by separation of the flow just ahead of the wing leading edge on the body. From the visual flow observations described in ref. 1, it was found that the subsonic flow behind the detached shock wave separated at the leading edge and formed a separation bubble on the wing upper surface. At the point of reattachment of the flow a shock wave was observed, and the existence of this is supported by the pressure distributions.

At values downstream of about $x/Ba = 2.5$ on the inboard half of the lower surface it can be seen (figs. 8,9,10) that the pressure is approximately constant. This can probably be attributed to a separation of the boundary layer in

the region of the adverse pressure gradient caused by the upstream influence of the root disturbance from the opposite wing. On the upper surface in this same region the effect of the corresponding disturbance is less marked. There is however some indication of an expansion beyond $x/Ba = 3$ but it is assumed that the main influence in this region will be caused by trailing edge effects.

(b) Spanwise pressure distribution

The chordwise results shown in figures 5 to 10 have been replotted as spanwise distributions in figure 11. It can be seen that the lower surface pressure distributions ahead of $x/Ba = 2.0$ are in fair agreement with Morikawa's theory except in the tip region. The upper surface pressure distributions on the other hand show the greatest discrepancies at both the root and tip regions.

(c) Chordwise distribution of normal force

These results are shown in figures 12 to 17. It can be seen that since the non-linear effects of incidence on both the upper and lower surfaces do not always cancel the discrepancies between experiment and theory are more marked than when the results are plotted separately for each surface. It is worth noting that linearised theory gives the local loading with reasonable accuracy.

(d) Tip pressure distribution - comparison with wing alone theory

The experimental pressure distributions near the wing tip, where the effect of the body upwash and body interference is small, are plotted in figures 44 and 45, and are compared as a matter of interest, with linearised theory for a wing alone having a span equal to the net semi-span. It is seen that fair agreement between the measured and theoretical pressure distributions exists on the lower surface but associated with the presence of the tip vortex, separation of the flow leads to the approximately constant pressure region on the upper surface.

(e) Comparison with other experimental data

At the present time few experimental investigations have been reported on the detailed pressure distribution on wings in the presence of bodies in supersonic flow. The few results quoted by Lawrence and Flax,[2] agree qualitatively with the present results. Similarly the results obtained by Pitts, Nielsen and Gionfriddo[18] for a wing of gross aspect ratio 3 are not dissimilar to those obtained here, although in our results the agreement with linear theory appears to be better and there is less scatter of the experimental results.

(ii) Roll angle $\phi = 30^\circ$

(a) Chordwise pressure distribution (figs 18-23)

These low incidence results have been plotted for both the upper and lower wings in terms of $B(C_p - C_{po})/a$ where $a = \theta \cos \phi$ and is equal to the true wing incidence. The results for 30° roll are in general in close agreement with the results for zero roll angle. The pressure distributions on the central portion of both wings (figures 19, 20 and 21) show good agreement with linearised theory for the smaller incidences. At incidences above 5°, more non-linearity is present than for the case of zero roll. The spanwise flow which develops at this angle of roll in conjunction with the crossflow over the body causes some separation of the flow in the region of the upper wing root, especially close to the leading edge (fig. 23). Near the tip of the upper wing the influence of the tip vortex is less marked than on the lower wing (fig. 18). In the latter case the tip vortex, moving in the stream direction, is swept on to the wing whereas on the upper wing the vortex is swept outboard from the tip.

(b) Spanwise pressure distributions

These results are plotted in fig. 24, and lead to similar conclusions to those stated in (ii)(a) above, and for $\phi = 0^\circ$ in paragraph (i)(b).

(c) Chordwise distribution of normal force (figs. 25 to 30)

The effect of the tip vortex on the lower wing now becomes more apparent. (Fig. 25). On the upper wing, near the root the leading edge separation arising from the body crossflow (fig. 30) is more marked than in the figures illustrating the separate pressure distributions.

(iii) Roll angle $\phi = 60^\circ$

(a) Chordwise pressure distribution

These results are plotted in the same way as for $\phi = 30^\circ$ and are shown in figs. 31 to 36. The results for the lower wing are in good agreement with those at $\phi = 0^\circ$ and 30° except in the tip regions, where the influence of the tip vortex is more apparent. The results for the upper wing show rather more variation with incidence than those for 30° and 0°, especially in the root region, due to the increased spanwise flow (fig. 36). It can be seen that near the root the upper surface suctions become much smaller than those predicted by linearised theory, as in this region the crossflow sweeping off the body causes

complete separation. Near the tip, as in the case of 30° roll, the influence of the tip vortex is reduced on the upper wing.

(b) Spanwise pressure distribution

These results are given in fig. 37. The variation with incidence in the upper wing pressure coefficients due to the increased spanwise flow at this roll angle is clearly seen. On the lower wing, however, the agreement with linearised theory is still reasonable.

(c) Chordwise distribution of normal force (figs. 38-43)

Near the tip of the lower wing the effects of the tip vortex found on the separate wing surfaces combine, to give normal force values which are considerably different from those given by linearised theory (fig. 38). Elsewhere the agreement is generally good.

8.2 Results at high incidences

(i) Roll angle $\phi = 0^\circ$

The chordwise pressure distributions for increments in incidence of 5° up to a maximum of 30° are plotted in figs. 46-51. Where possible the appropriate leading edge pressures calculated from shock expansion theory are given. The corresponding spanwise pressure distributions are shown in fig. 52.

It can be shown that the leading edge shock wave from a 6° total angle wedge allowing for body upwash becomes detached at the Mach number of these tests at incidences above about 10° at the root and 17° at the tip. It has, therefore, not been possible to calculate leading edge values for incidences in excess of these by shock expansion theory. At incidences where the shock wave is detached, large values of C_p on the lower surface were measured close to the leading edge.

As the incidence is increased, the Mach number behind the leading shock wave on the lower surface decreases, and consequently the quasi-two dimensional region between the root and tip Mach lines contracts. This is clearly shown in figs. 46-50.

From the pressure measurements close to the leading edge, it was observed that the pressures on the lower surface were lower than shock-expansion values near the root, but the agreement became progressively better towards the tip. It is suggested that this is due to the reduction in body upwash caused by the downwash from the symmetric vortex pair above the body.

An interesting feature of these pressure distributions is the region of approximately constant pressure over the complete upper surface. At 30° incidence the pressure coefficient approaches the value of $C_p = -0.357$, which corresponds to zero absolute pressure. Thus at large angles of incidence it is the lower surface pressure that largely controls the lift on the wing. The spanwise pressure distributions shown in fig. 52 show clearly the nearly constant pressure regions on the upper surface as well as the reduction in pressure on the lower surface towards the tips.

(ii) Roll angle $\phi = 30^\circ$

The chordwise pressure distributions are shown in figs. 53 to 58 and the corresponding spanwise distributions are plotted in fig. 59.

The effects noted in the discussion at $\phi = 0^\circ$ occur also for this angle of roll. In addition marked differences in the pressure distributions between the lower surfaces of the upper and lower wings, especially near the root, are noted as the incidence increases. This effect is clearly indicated in figs. 58 and 59 and is the result of the separation of the spanwise flow on the leeward side of the body.

On the upper surface of the lower wing a marked fall in pressure occurs at positions on the wing close to the leading edge at the tip (fig. 53) and progressively further downstream to 0.4c at the root (fig. 58). It is suggested that this is the result of the influence of the tip vortex sweeping over the wing surface.

(iii) Roll angle $\phi = 60^\circ$

The chordwise pressure distributions are shown in figs. 60 to 65 and the corresponding spanwise distributions are plotted in fig. 66.

The main feature indicated by these pressure distributions is the high values of pressure on the lower surface of the lower wing as compared with the magnitudes of the pressures on the three other surfaces. This fact will assist in explaining the large rolling moments present on this type of wing-body combination at large angles of roll and incidence.

The marked fall in pressure which exists on the upper surface of the lower wing is clearly more extensive than in the case at $\phi = 30^\circ$ and is again presumably due to the tip vortex sweeping over a greater area of the wing surface.

Near the root of the upper surface of the upper wing the pressure distribution is influenced by the proximity of the body vortices. On the lower surface of the upper wing the considerable reduction in pressures (see figs. 62, 63, 64, 65 and 66) over the whole surface is probably associated with an additional separation of the flow from the body.

(iv) Roll angle $\phi = 90^\circ$

The chordwise pressure distributions for one surface only are given in figs. 67 to 72 and the corresponding spanwise distributions are shown in fig. 73.

The pressures on the lower wing, apart from those close to the tip, show a regular increase with incidence which is presumably a sweepback effect. The suctions near the wing tip (fig. 67) are due to separated flow associated with the finite tip thickness.

At high angles of incidence more and more of the upper wing will be washed by the body vortices. Their spread, as the incidence increases, is most clearly seen from the pressure distribution for 20° incidence in fig. 67. This explains why the pressures on the upper wing are predominantly negative.

8.3 Overall forces and moments

N.B. All force and moment coefficients are based on net wing area.

(i) Normal Force

From fig. 74 it will be seen that the variation of normal force coefficient C_N with angle of pitch is almost linear at high angles of incidence except for $\phi = 60^\circ$ (upper wing). This result is not at all obvious from the discussion of the detailed pressure distributions, especially as the non-linear effects on the pressures are so large. It appears that although the suctions on the upper surface hardly increase with incidence, the pressures on the lower surface increase rapidly, resulting in a pressure difference which is approximately linear with incidence.

In fig. 75, the normal force results for 0° roll are compared with the various theoretical predictions described in §7. It will be seen that reasonable agreement is obtained with the curve given by Flax and Lawrence's empirical relation for viscous flow over a wing of small aspect ratio, when this

is modified to allow for the effect of the body. The interference factor used for this correction, again empirical, is that given by Nielsen and Kaattari[13]. The upper curve, which rather overestimates the experimental results, is that obtained from a similar relation given by Cheng for viscous flow, modified by the aforementioned interference factor. The two lower curves are obtained from linearised theory and from Nielsen and Kaattari's empirical relation. Neither of these takes account of viscous effects, and so it is not surprising that they show reasonable agreement only for the low incidence results.

(ii) Centre of Pressure

Figure 76 shows the chordwise and spanwise positions of the centre of pressure at the angles of roll 0°, 30° and 60°. It will be seen that the chordwise position of the centre of pressure is practically unchanged with roll angle over the whole range of incidence. The shift in centre of pressure with incidence is from approximately 0.25c at 0° to 0.45c at 30° incidence. The shift is very small above 20° incidence. It should be noted that although the centre of pressure position on the complete wing is almost independent of roll, the same is not true of the centres of pressure of each half-wing (Figs. 77 and 78).

The spanwise position of the centre of pressure at $\phi = 0^\circ$ is approximately constant at 0.65 of the gross semi span above 10° incidence. At $\phi = 30^\circ$ and 60° a small outboard movement of the centre of pressure occurs on each wing.

In figure 76 are shown the co-ordinates of the centre of pressure at 0° roll given by linearised theory for a wing alone having an aspect ratio equal to the net aspect ratio of the wing-body combination. These are 0.624 of the gross semi-span in a spanwise direction from the centre line, and 0.25c from the leading edge. A curve showing the estimated chordwise movement of the centre of pressure with incidence is also shown. This was obtained from an empirical relation given in ref. 14. for the effects of viscosity on the normal force and pitching moment. The normal force due to these viscous effects acts in the region of the half-chord point, and so moves the centre of pressure aft at high incidences.

(iii) Lift, drag and sideforce coefficients

Figure 79 shows the variation of lift coefficient, C_L, with incidence for various values of sideslip angle β. Also shown on this graph is the linearised theory result for a wing alone having an aspect ratio equal to the gross aspect ratio of the wing body combination. The present experimental results show that the lift curves are slightly non-linear at small angles of incidence, but at larger angles of incidence the results are linear. (Although when extrapolated back the curves do not pass

through the origin). It will be seen that the variation in the C_L vs α curves with sideslip is less than about 10 per cent up to 15° sideslip, the greatest variation occurring at the smaller sideslip angles. It can be seen that the linearised theory result for the wing alone underestimates the present experimental results by about 25 per cent.

Figure 80 shows the variation of drag coefficient, C_D, with incidence and sideslip. The effect of sideslip on C_D appears to be similar to that on C_L, and again the linearised theory result for the wing alone underestimates the experimental results by about 25 per cent.

Figure 81 shows the results obtained for the variation of the side force coefficient C_Y with sideslip and incidence. The variation of C_Y with incidence is approximately linear at small angles of incidence. It should be noted, as mentioned above, that the side force results have been obtained by integration of pressures on the wing surfaces, and do not include the forces on the tips.

(iv) Spanwise distribution of normal force

The spanwise distributions of normal force at angles of roll 0°, 30° and 60° are shown in fig. 85. It can be seen that at 0° roll and small incidences the distribution approximates to the elliptic distribution predicted by slender body theory[15]. At higher incidences the tip effects give increased loadings on the outboard portion of the wings which results in the spanwise distribution of normal force being more rectangular. Above 15° incidence the effects of separation near the root cause a reduction of loading there but over the outboard portion of the wing the normal force remains approximately constant.

At roll angles of 30° and 60° similar effects are noted at small angles of incidence but above about 5° incidence separation on the upper wing causes large changes in the magnitude and distribution of the normal force. The effects of this on the rolling moment are discussed in the following paragraph.

(v) Pitching and Rolling moment coefficients

Figure 82 shows the variation of pitching moment coefficient with incidence for various angles of sideslip, and figs. 83 and 84 the variation of rolling moment coefficient with angles of roll, pitch and sideslip, incidence respectively. These results are for the two half-wings in combination.

It can be seen that the variation of pitching moment with incidence is rather non-linear with incidence above about 5°. This is due more to the non-linearity in the normal force at small incidences than to the centre of pressure movement.

In fig. 83 only four values of rolling moment (including those at 0° and 90° roll) are available for each angle of pitch, since measurements have only been taken at intervals of 30° roll angle, and therefore only tentative conclusions can be drawn from these curves. However it can be seen that the rolling moment rises to a maximum in the region of ϕ = 60° and increases almost linearly with incidence.

These effects are evident from the spanwise distributions of normal force shown in fig. 85. At a given roll angle, the spanwise flow over the lower wing sweeps round the body, and separates near the root of the upper wing. The position of flow reattachment on the upper wing moves outboard as the incidence and roll increase. At 30° roll it can be seen that the spanwise centre of pressure is approximately the same on both the upper and lower wings at all incidences. Since the normal forces are of similar magnitude, the resulting rolling moments are very small. At 60° roll and small incidences although the normal forces are of similar magnitude, the spanwise centres of pressure on the two wings are different, giving an appreciable rolling moment. At larger incidences the flow is separated over most of the upper wing as described above, and the consequent large reduction in normal force on this wing results in a large rolling moment. It should be noted, however, that a study of the detailed pressure distributions shows the flow to be separated over most of the upper surface of the lower wing. Hence the rolling moment at 60° roll and large incidence is primarily due to the large positive pressures on the lower surface of this wing. These results are clearly relevant to the consideration of the rolling moment that occurs on wing-body combinations having cruciform or other wing arrangements.

9. Acknowledgements

The authors are indebted to Professor A.D. Young for his assistance in formulating the programme, and for his help in the discussion of the experimental results; Mr. S.H. Lilley for preparation of the model and apparatus and supervision of the tunnel; English Electric Co. Ltd. for the supply of the model and general encouragement and support; and to the Ministry of Supply who sponsored this investigation. In addition the authors wish to acknowledge with thanks the co-operation and assistance received from all those responsible for the amassing and reduction of the experimental results and for taking part in the numerous discussions at all stages in this investigation. Space alone prevents individual acknowledgement.

10. Conclusions

Measurements have been made of the pressure distribution on a 6° single wedge low aspect ratio wing mounted on a cylindrical body with an ogival nose. The tests were made at a Mach number of 2.0, at incidences from 0° to 30°, and roll angles of 0°, 30°, 60° and 90°. The results are compared with various theoretical predictions, and the following conclusions reached.

(i) Behind the Mach waves from the leading edge tip and root, the pressure distributions on both wing surfaces show good agreement, for small angle of incidence, with values given by Morikawa's approximate solution, modified to allow for the effects of the tip.

(ii) At the wing leading edge, the pressure coefficients are predicted reasonably well by shock expansion theory, assuming an upwash distribution, due to an infinite cylindrical body, acting on the wing. Near the root, at higher angles of incidence, the upwash is reduced by the effect of the body vortices, and so in this region the pressures are overestimated by this method.

(iii) It was found that viscous effects have considerable influence on the pressure distributions, especially in the regions of the wing tip, root, and those areas which are influenced by disturbances from the opposite wing.

(iv) The non-linear effects of incidence on the pressure coefficients largely cancel out when the results are integrated for the two wing surfaces, and the resulting normal force and lift curves are roughly linear at the higher incidences, (except for the upper wing at 0° roll). The residual non-linear effects on normal force and centre of pressure can be explained in terms of the viscous cross-flow over a wing of small aspect ratio. When the latter effects are included, the measured normal force agrees fairly well with that predicted by the empirical relation of Nielsen and Kaattari and the slender body result.

(v) At roll angles of 30° and 60°, more non-linearity is found in the pressure results than for 0°, and the flow over the upper wing shows evidence of partial or complete separation. Under these conditions, at high angles of incidence, it is shown that the forces and moments on the wing are governed almost entirely by the large positive pressures on the under surface of the lower wing. This results in a rolling moment which increases rapidly with roll angle, to a maximum in the region of 60° roll.

APPENDIX I

Discussion of the linearised supersonic flow theory of wing-body interference.*

Introduction

A short discussion on the linearised theory of wing-body interference at supersonic speeds is presented for the restricted case of a wing of zero thickness and infinite span mounted far from the nose of a cylindrical body of circular cross-section. A solution for the perturbation velocity potential in terms of an integral equation is compared with the methods of Morikawa[8], Chester[10], Nielsen[9], Bolton-Shaw[6], and Ferrari[7]. A more complete discussion on some of these methods is given in the extensive review on this subject by Lawrence and Flax.[14]

It is noted that this problem of wing body interference is analogous to a diffraction problem in which the diffraction of waves around a rigid semi-circular cylinder results from prescribed impulsive motion of the planes $Y = 1$ to ∞ and $Y = -1$ to $-\infty$.

Analysis

Consider a wing, in the form of a semi-infinite plate, mounted on the axis of an infinitely long circular cylinder. The wing and body are at the common small incidence, α, to the free-stream direction, defined by the velocity u_∞. (The effects of wing thickness and finite span are not considered. The latter problem is discussed in Appendix II, whilst a discussion on the former problem can be found in reference 10). The flow is known everywhere upstream of the wing leading edge and on the wing and body the normal velocity must be zero.

Let x be measured along the body axis with origin at the point of intersection with the wing leading edge extended through the body. Let the wing leading edge be the y-axis so that the wing lies in the (x,y) plane with the z-axis normal to it.

According to linearised theory[8] this problem can be replaced by superposition of the solutions to (a) the body alone at incidence α and (b) the wing, at an incidence $\bar{\alpha}$, mounted on

---

* The authors wish to thank Professor G.N. Ward and Mr. D.J. Green for certain suggestions relating to the preparation of this Appendix.

the body at zero incidence, where $\bar{a}$ is equal to the incidence a plus an apparent twist imposed by the original upstream flow induced by the body at incidence.

The solution to problem (a) in terms of the perturbation velocity potential, ϕ, (neglecting the component of flow parallel to the body axis), is

$$\phi = u_o \, a \, r \sin\theta \left(1 + \frac{a^2}{r^2}\right)$$

where r, θ, x are cylindrical polar coordinates and (a) is the body radius. Since this solution is independent of x it contributes nothing to the pressure component.

The boundary conditions for problem (b) are

$$\phi_r \ (a,\theta,x) = 0$$

$$\frac{\phi_\theta}{r} \ (r,0,x) = - u_o a \left(1 + \frac{a^2}{r^2}\right) \quad x > 0 \qquad \text{.....(1)}$$

where ϕ satisfies the wave equation

$$\phi_{rr} + \frac{\phi_r}{r} + \frac{\phi_{\theta\theta}}{r^2} - B^2 \phi_{xx} = 0 \qquad \text{.....(2)}$$

and $B = \sqrt{M^2 - 1}$, M is the freestream Mach number.

If $R \equiv r/a$ and $X \equiv x/Ba$ the boundary conditions (1), on the body, will be applied at $R = 1$ and equation (2) becomes

$$\phi_{RR} + \frac{\phi_R}{R} + \frac{\phi_{\theta\theta}}{R^2} - \phi_{XX} = 0 \qquad \text{.....(3)}$$

The pressure coefficient, C_p, is determined from

$$\frac{BC_p}{a} = \frac{-2}{au_o a} \frac{\partial\phi}{\partial X} .$$

Following Morikawa (reference 8) the Laplace transform $\bar{\phi}$, of ϕ with respect to the freestream direction, X, is given by

$$\bar{\phi}\,(R,\theta;p) = -\frac{1}{2\pi} \int_c \left(\bar{\phi} \frac{\partial G}{\partial n} - G \frac{\partial \bar{\phi}}{\partial n}\right) dl \qquad \text{.....(4)}$$

where $\bar{\phi}(R,\theta;p) = \int_0^\infty e^{-pX}\,\phi(R,\theta,X)\,dX$, and

G is a Green's function for the transformed wave equation having the boundary C. $\bar{\phi}$ and its outward normal derivative $\bar{\phi}_n$ are related on the boundary C. From the boundary conditions stated

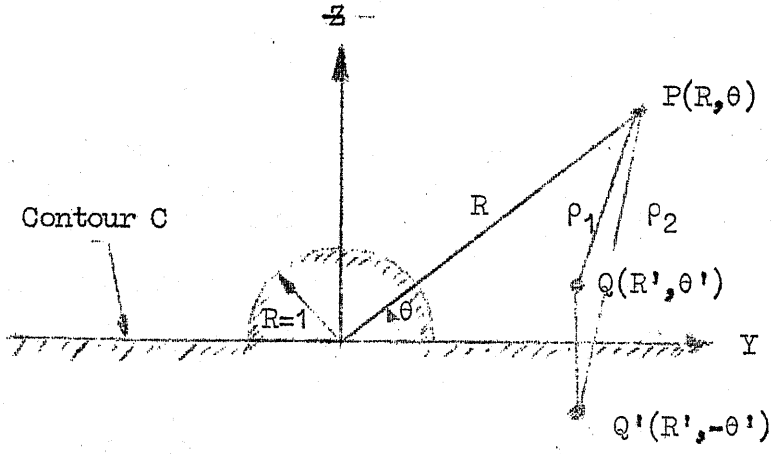

in equation (1) $\bar{\phi}_n$ is zero on the body (R = 1) and is equal to

$$\frac{a\,u_o\,a}{p}\left(1 + \frac{1}{R^2}\right) \quad \text{on the wing.}$$

A fundamental solution of the transformed wave equation for a fixed point $P(R,\theta)$ and a variable point $Q(R',\theta')$ is $K_o(p\rho_1)$, where $\rho_1^2 = R^2 + R'^2 - 2RR'\cos(\theta-\theta')$ is the distance PQ, and K_o is the modified Bessel function of the second kind. Hence the Green's function, satisfying the boundary condition $\partial G/\partial n = 0$ on the wing is

$$G_1(R,\theta;R',\theta') = K_o(p\rho_1) + K_o(p\rho_2) \qquad \text{.....(5)}$$

where $\rho_2^2 = R^2 + R'^2 - 2RR'\cos(\theta+\theta')$ is the distance between P and the reflection of Q in the Y axis. The Green's function for which $\partial G/\partial n = 0$ on both the wing and body is

$$G_2(R,\theta;R',\theta') = K_o(p\rho_1) + K_o(p\rho_2) - 2\left[\frac{I_o'(p)}{K_o'(p)}\,K_o(pR)\,K_o(pR') + 2\sum_1^\infty \frac{I_n'(p)}{K_n'(p)}\,K_n(pR)\,K_n(pR')\cos n\theta\,\cos n\theta'\right] \qquad \text{.....(6)}$$

Case A The value of $\bar{\phi}$ and ϕ_X obtained from G_1

If G_1 obtained from equation (5) is substituted into equation (4) together with the values of ϕ_n on the wing and body then

$$\bar{\phi}(R,\theta;p) = \frac{au_o a}{2\pi p}\int_1^\infty \left(1+\frac{1}{R'^2}\right)\left[G_1(R,\theta;R',\pi)+G_1(R,\theta;R',0)\right]dR'$$

$$+\frac{1}{2\pi}\int_o^\pi \bar{\phi}(1,\theta';p)\frac{\partial G_1}{\partial R'}(R,\theta;1,\theta)\,d\theta' \quad \ldots(7)$$

$$= \frac{au_o a}{\pi p}\int_1^\infty \left(1+\frac{1}{R'^2}\right)\left[K_o\left(p\left\{R^2+R'^2-2RR'\cos\theta\right\}^{\frac{1}{2}}\right)\right.$$

$$\left. + K_o\left(p\left\{R^2+R'^2+2RR'\cos\theta\right\}^{\frac{1}{2}}\right)\right]dR'$$

$$-\frac{p}{2\pi}\int_o^\pi \bar{\phi}(1,\theta';p)\left[\frac{K_1\left(p\left\{R^2+1-2R\cos(\theta-\theta')\right\}^{\frac{1}{2}}\right)(1-R\cos(\theta-\theta'))}{\left\{R^2+1-2R\cos(\theta-\theta')\right\}^{\frac{1}{2}}}\right.$$

$$\left. + \frac{K_1\left(p\left\{R^2+1-2R\cos(\theta+\theta')\right\}^{\frac{1}{2}}\right)(1-R\cos(\theta+\theta'))}{\left\{R^2+1-2R\cos(\theta+\theta')\right\}^{\frac{1}{2}}}\right]d\theta'$$

$$\ldots\ldots\ldots\ldots(8)$$

The appropriate inverse Laplace transforms, written $\mathcal{L}^{-1}$, are

$$\left.\begin{aligned}\mathcal{L}^{-1}\left\{p\bar{\phi}\,;X\right\} &= \phi_X\\ \mathcal{L}^{-1}\left\{p^2\bar{\phi}\,;X\right\} &= \phi_{XX}\end{aligned}\right\} \quad \ldots\ldots\ldots\ldots(9)$$

$$\left.\begin{aligned}\mathcal{L}^{-1}\left\{K_o(pa)\,;X\right\} &= \frac{1}{\sqrt{X^2-a^2}} \qquad X>a\\ &= 0 \qquad\qquad 0<X<a\end{aligned}\right\} \quad \ldots\ldots(10)$$

$$\mathcal{L}^{-1}\left\{K_1(pa)\ ;\ X\right\} = \frac{X/a}{\sqrt{X^2 - a^2}} \qquad X > a$$
$$= 0 \qquad 0 < X < a \Bigg\} \quad \ldots\ldots\ldots(11)$$

and from the product theorem

$$\mathcal{L}^{-1}\left\{F_1(p)\ F_2(p)\right\} = \int_0^X f_1(\xi)\ f_2(X-\xi)\ d\xi \quad \ldots\ldots\ldots(12)$$

where $\mathcal{L}^{-1}\left\{F_{1,2}(p);\ X\right\} = f_{1,2}(X)$.

Hence the transformed solution in Cartesian coordinates on the wing surface becomes

$$\phi_X\ (X,Y,0) = \frac{au_o a}{\pi}\left(\int_1^{X+Y} + \int_{Y-X}^{-1}\right)\left(1 + \frac{1}{\eta^2}\right)\left[X^2-(Y-\eta)^2\right]^{-\frac{1}{2}}\ d\eta$$

$$- \frac{1}{\pi}\int_0^{X-Y+1}\int_0^{\Psi} \frac{\phi_{\xi\xi}(1,\theta',\xi)(1 - Y\cos\theta')(X-\xi)\ d\theta'\ d\xi}{(Y^2+1-2\ Y\cos\theta')\left[(X-\xi)^2-Y^2-1+2\ Y\cos\theta'\right]^{\frac{1}{2}}}$$

where $\cos\Psi = \dfrac{Y^2 + 1 - (X-\xi)^2}{2Y}$.

Similarly on the body (R=1) the transformed solution becomes

$$\phi_X(1,\theta,X) = \frac{au_o a}{\pi}\left(\int_1^{\eta_1} + \int_{\eta_2}^{-1}\right)\left(1 + \frac{1}{\eta^2}\right)\left[X^2 - 1 - \eta^2 + 2\eta\cos\theta\right]^{-\frac{1}{2}}\ d\eta$$

$$- \frac{1}{4\pi}\int_0^X\int_{-\pi}^{\pi} \frac{\phi_{\xi\xi}(1,\theta',\xi)(X-\xi)d\theta'\ d\xi}{\left[(X-\xi)^2 - 2(1-\cos(\theta-\theta')\ )\right]^{\frac{1}{2}}} \quad \ldots\ldots\ldots(14)$$

where $\eta_1, \eta_2 = \cos\theta \pm \sqrt{X^2 - \sin^2\theta}$

and the third integral in equation (14) is taken over the area shown in the diagram below. It should be possible to obtain a solution of these integral equations by the use of numerical methods.

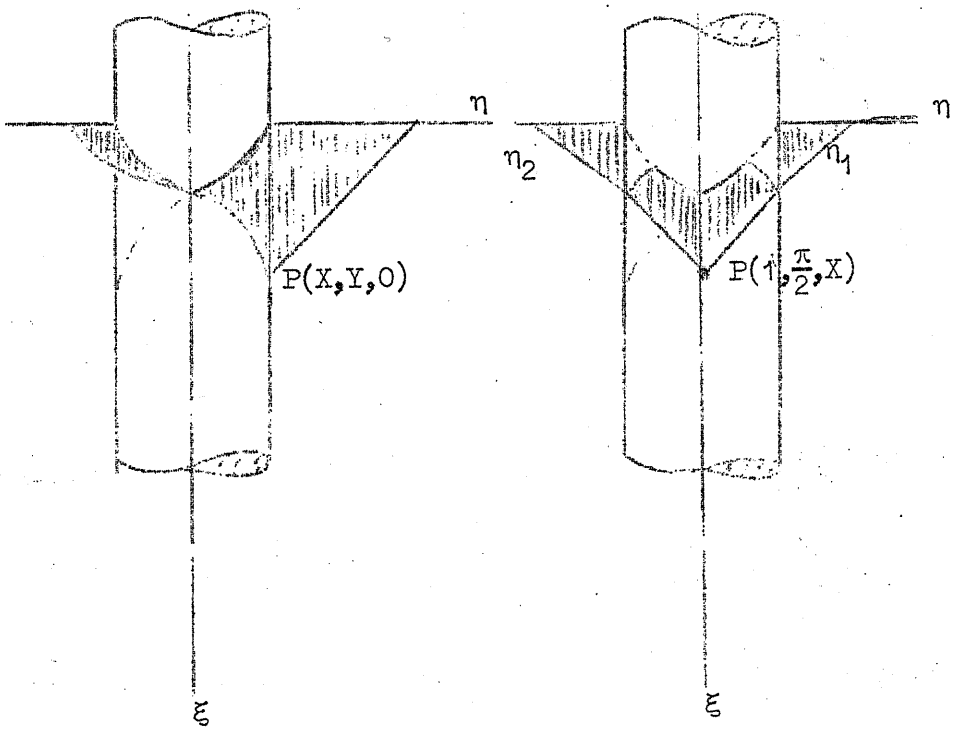

(Wing solution) (Body solution)

It should be noted that the third integral of equation (13), which represents the body contribution to the wing potential, is zero outside the influence of the characteristic $\xi = \eta - 1$. In addition, this integral and the corresponding integrals in equation (14), have zero integrands in the region ahead of the characteristics from the wing leading edge-body junction, since $\phi_{\xi\xi}$ is zero in this region.

The boundaries for the regions of integration in the above integrals do not correspond to the paths of the Mach lines from the wing leading edge except in the region outside the influence of the body. The reason for this lies in the choice of the Green's function, where, as a result, the body integral represents a correction to the wing integral to satisfy the condition of zero normal velocity on the body surface. The paths of the Mach lines are shown in the diagram below.

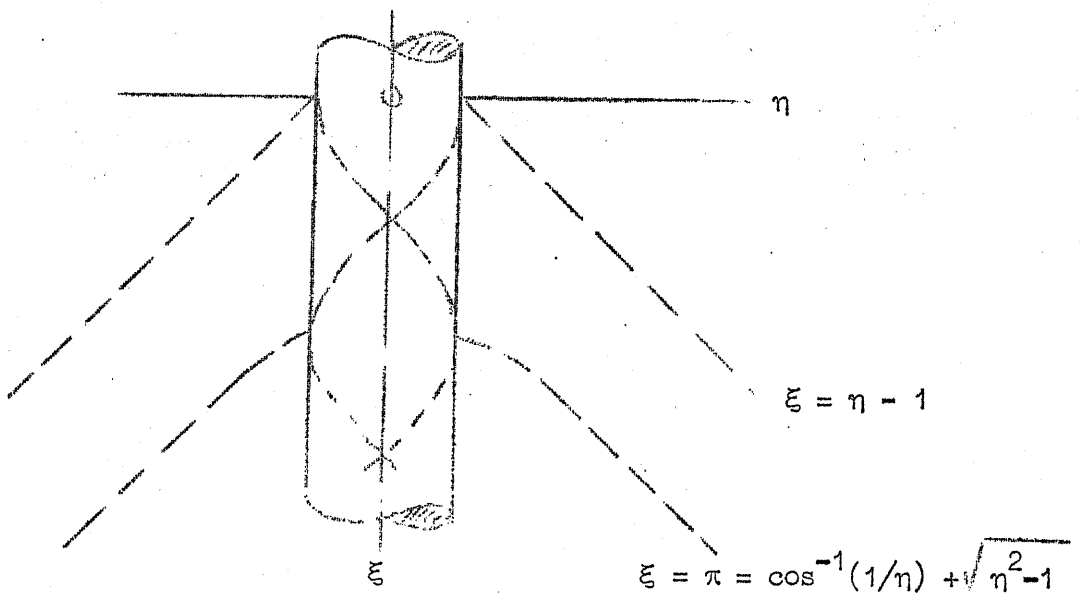

Case B. The value of $\bar{\phi}$ and ϕ_X obtained from G_2. (Morikawa's Solution)

If we use the second form of the Green's function given in equation (6) then

$$\bar{\phi}(R,\theta;p) = \frac{au_o a}{\pi p}\int_1^\infty \left(1+\frac{1}{R'^2}\right)\left[K_o\left(p\left\{R^2+R'^2-2RR'\cos\theta\right\}^{\frac{1}{2}}\right)\right.$$

$$\left. + K_o\left(p\left\{R^2+R'^2+2RR'\cos\theta\right\}^{\frac{1}{2}}\right)\right]dR'$$

$$-\frac{2au_o a}{\pi p}\int_1^\infty \left(1+\frac{1}{R'^2}\right)\left[\frac{I_o'(p)}{K_o'(p)}K_o(pR)K_o(pR')\right.$$

$$\left. + 2\sum_1^\infty \frac{I_{2n}'(p)}{K_{2n}'(p)}K_{2n}(pR)\,K_{2n}(pR')\cos 2n\theta\right]dR'$$

$$= \bar{\phi}^{(1)} + \bar{\phi}^{(2)} \qquad \text{.....(15)}$$

where Morikawa refers to $\bar{\phi}^{(1)}$ as the 'flat plate' solution and $\bar{\phi}^{(2)}$ as the 'body' solution.

The transformed solution for $\phi_X^{(1)}$ is identical with

the wing integrals in equations (13) and (14). This solution is equivalent to that of the wing alone in the presence of the body upwash, where the body is replaced by an extension of the wing set at zero incidence.

Morikawa shows that difficulties arise when the inverse Laplace transform of $\bar{\phi}^{(2)}$ is attempted. He finds that an upper limit for the 'body' solution $\phi_X^{(2)}$ is obtained when the body is replaced by a reflection plane situated at the position of the wing-root-body junction. (This naturally simulates the case of a body of infinite radius). Morikawa also derives an approximate expression for $\phi_X^{(2)}$ in the vicinity of the wing leading edge - body junction. Although the error in $\phi_X^{(2)}$ is not estimated Morikawa shows that it approaches the correct asymptotic value for large X. Morikawa's calculated results for the chordwise pressure distribution in the wing root-body junction are shown in figure 86. There results have been crudely extended to the region where the wing pressures are influenced by disturbances from the opposite wing. Figure 86 also shows the calculated results for the 'reflection plane' solution and when the body is replaced by an extension of the wing at both an incidence of zero and 2α. The latter solution constitutes the pressure distribution obtained from the sum of the first and second integrals in Chester's solution.

Chester's method

An approximate solution for the velocity potential has been obtained by Chester[10] which has the merit that the order of the error terms are estimated at each stage. In this method the potential, ϕ, is expressed in the form

$$\phi = \phi_W + \phi_B$$

where ϕ_W is the wing alone potential when the wing is extended through the body and ϕ_B constitutes the interference velocity potential. The boundary conditions applied to ϕ_B are equivalent to those in Nielsen's method discussed below. Although this formulation of the wing-body interference problem is different from that adopted above it can be shown that in our notation,

$$\phi_X(X,Y,0) = \frac{au_o a}{\pi}\left(\int_1^{X+Y} + \int_{Y-X}^{-1}\right)\left(1+\frac{1}{\eta^2}\right)\left[X^2-(Y-\eta)^2\right]^{-\frac{1}{2}}\,d\eta$$

$$+\frac{2au_o a}{\pi}\int_{Y-X}^{1}\frac{d\eta}{\sqrt{X^2-(Y-\eta)^2}}$$

$$-\frac{2au_o a}{\pi}\int_{\frac{Y^2+1-X^2}{2Y}}^{1}\frac{d\eta}{\sqrt{X^2-Y^2-1+2Y\eta}}$$

where in the third integral $-1 \leq (Y-X) \leq 1$ and in the fourth integral

$$-1 \leq \frac{Y^2 + 1 - X^2}{2Y} \leq 1.$$

The first and second integrals represent the contribution due to the wing in the presence of the body upwash. The third integral is the contribution from the portion of the equivalent wing inside the body. This equivalent wing is set at twice the incidence of the true wing. The last integral represents a correction to the third integral to allow for the smaller influence of the body than is exerted by the equivalent wing.

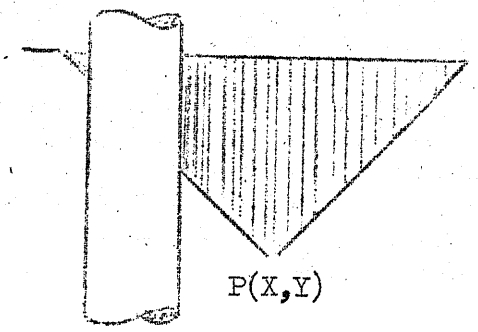

(a) (Wing integration)

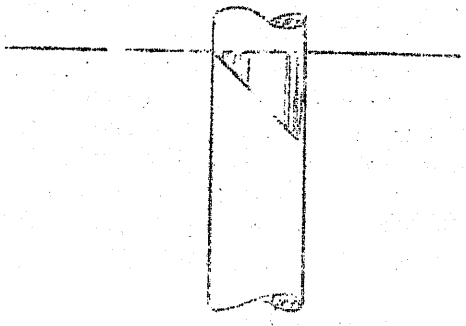

(b) (Equivalent wing integration)

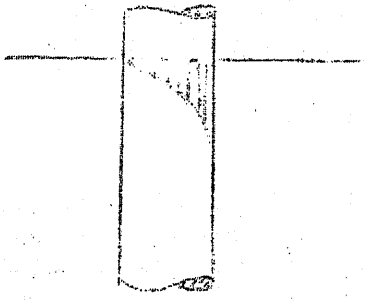

(c) (Body integration)

It can be seen from equations (13) and (16) that the 'wing contribution' to $\emptyset$ in equation (16) is identical with that given in equation (13), whereas the 'body contribution', represented by the third and fourth integrals on the R.H.S. of equation (16), approximates to the correct expression given by the third integral on the R.H.S. of equation (13). Numerical calculations show that $\emptyset_Y$ obtained from equation (16) is very sensitive to values of the fourth integral, which according to the assumptions made in the formulation of the approximate boundary conditions, presents the source of greatest

error in this method in the region of the wing root leading edge - body junction. The calculated results for the chordwise pressure distribution in the wing root - body junction are shown in figure 86. The upper curve (1) represents the sum of the three integrals when the area of integration in (c) is taken downstream of the root Mach line, whereas for the lower curve (2) the area of integration in (c) is taken downstream of the wing leading edge extension inside the body.

Method of Nielsen

Nielsen[9] considers the problem of a rectangular wing mounted at incidence on an infinite cylindrical body of circular cross-section at zero incidence. The potential ϕ is expressed in the form

$$\phi = \phi_W + \phi_B$$

where ϕ_W represents the wing alone solution with the wing extended through the body. On the wing, outside the region influenced by the wing tips, $\partial\phi_W/\partial z = -u_o a$ and the corresponding normal flow at $R = 1$ is given by $\partial\phi_W/\partial R = -u_o a \sin\theta$. Since $\partial\phi/\partial R = 0$ at $R=1$ the interference potential, ϕ_B, must satisfy the boundary conditions

$$\left(\frac{\partial\phi_B}{\partial R}\right)_{R=1} = u_o\, a \sin\theta \quad \text{and} \quad \left(\frac{\partial\phi_B}{\partial\theta}\right) = 0 \quad \text{on} \quad \theta = 0,\pi \quad \text{for} \quad Y \geq 0.$$

Thus so far Nielsen's method is identical with that of Chester, except that in the latter case the potential ϕ_W is influenced by both the body at zero incidence and the upwash due to body incidence. At this point the two solutions diverge. In Chester's method the value of ϕ_B is obtained from the slender-body approximation to the appropriate Green's function whereas Nielsen expresses ϕ_B in terms of a Fourier cosine series in the meridional angle. The final solution for ϕ_B, in Nielsen's method, is obtained from the Laplace transform method in which the inverse Laplace transform is evaluated in terms of a new function, $M_{2n}(X)$, involving the modified Bessel functions K_{2n}. It is pointed out by Lawrence and Flax [14] that the Green's function employed by Morikawa could be used to obtain the same results. Thus the inverse Laplace transform which Morikawa was unable to evaluate, can be expressed in terms of the Nielsen function M_{2n}.

From calculations made by Nielsen and others, it appears that a very large number of terms in the Fourier cosine series is required, especially close to the leading edge, in order to obtain accurate pressure distributions. In view of the fair agreement between the experimental pressure distributions reported above and the calculated values obtained from Morikawa's approximate solution,

together with the appreciation of the basic limitations of a linearised theory solution, it appeared unjustified in the present instance to devote a further considerable effort to the calculation of more accurate theoretical results on the lines suggested by Nielsen. The value of the chordwise pressure distribution in the wing root - body junction, as given by Nielsen and Pitts[17], is shown in figure 86. It differs from that given by the Morikawa approximate solution by about 10 per cent except close to the leading edge where it coincides with both Morikawa's and Chester's solutions.

Method of Bolton-Shaw

Bolton-Shaw[6] considers the same problem as Nielsen in which a rectangular wing at incidence is mounted on an infinite circular cylinder set at zero incidence. The solution for ϕ in series form is obtained by the method of separation of variables, in which the boundary conditions on the body and the wing are satisifed at a finite number of selected control points. However as yet no numerical calculations are available and the rapidity of the convergence of the infinite series has not been investigated.

Method of Ferrari

Ferrari[7] considers the general case of arbitrary wing - body configuration for which the wing alone and body alone solutions are known. The method, which is an iterative one, involves the calculation of the potential, ϕ, expressed in the form

$$\phi = \sum_{k=0}^{N} \phi_W^{(k)} + \phi_B^{(k)}$$

where $\phi_W^{(k)}$ and $\phi_B^{(k)}$ satisfy boundary conditions on the wing alone and body alone respectively. However insufficient numerical calculations are at present available to make a reliable comparison between Ferrari's results and those obtained from the other methods and from experiment.

APPENDIX II

The pressure distribution on the wings including the effect of body upwash

The pressure coefficient, C_p, is given by

$$C_p = \frac{p-p_o}{\frac{1}{2}\rho_o u_o^2} = -\frac{2}{u_o}\frac{\partial \phi}{\partial x} \qquad \ldots\ldots\ldots\ldots(1)$$

where[19]

$$\phi(x,y,z) = -\frac{1}{\pi}\iint \frac{\partial \phi}{\partial z_o}(x_o,y_o,0)\,\frac{dx_o\,dy_o}{\sqrt{(x-x_o)^2-B^2\{(y-y_o)^2+z^2\}}} \qquad \ldots\ldots\ldots\ldots(2)$$

x is measured in the stream direction with its origin at the intersection of the leading edge (y axis) in the plane of symmetry and

$$x_o \leqslant x - B\sqrt{(y-y_o)^2 + z^2}$$

The value of $\partial\phi/\partial z_o$ in the plane $z_o = 0$ is found from

$$\frac{\partial \phi}{\partial z_o}(x_o,y_o,0) = -u_o\,\bar{a}\,(x_o,y_o,0) \qquad \ldots\ldots\ldots\ldots(3)$$

where $\bar{a}$ is the combined incidence and apparent twist due to the body upwash. If the body is an infinitely long circular cylinder having the same incidence, a, as that of the wing, which is taken to be of zero thickness, then

$$\bar{a}\,(x_o,y_o,0) = a\left(\frac{a^2}{y_o^2}+1\right) \qquad \ldots\ldots\ldots\ldots(4)$$

Thus from equations (1), (2), (3) and (4)

$$C_p = -\frac{2a}{\pi}\frac{\partial}{\partial x}\iint\left(\frac{a^2}{y_o^2}+1\right)\frac{dx_o\,dy_o}{\sqrt{(x-x_o)^2-B^2(y-y_o)^2}} \qquad \ldots(5)$$

where $B(y-y_o) \leqslant (x-x_o)$.

If we write $\lambda = \dfrac{x-x_o}{B\,a}$ and $\eta = \dfrac{B(y_o-y)}{B\,a}$

then, together with $X = \frac{x}{Ba}$ and $Y = \frac{y}{a}$, equation (5) becomes

$$\frac{BC_p}{a} = \frac{\partial}{\partial X} \int d\lambda \int F(\lambda,\eta)\, d\eta \qquad \text{.....(6)}$$

where

$$F(\lambda,\eta) = \frac{2}{\pi}\left(1 + \frac{1}{\{Y+\eta\}^2}\right)\frac{1}{\sqrt{\lambda^2 - \eta^2}} \quad .$$

Case (i) Infinite wing

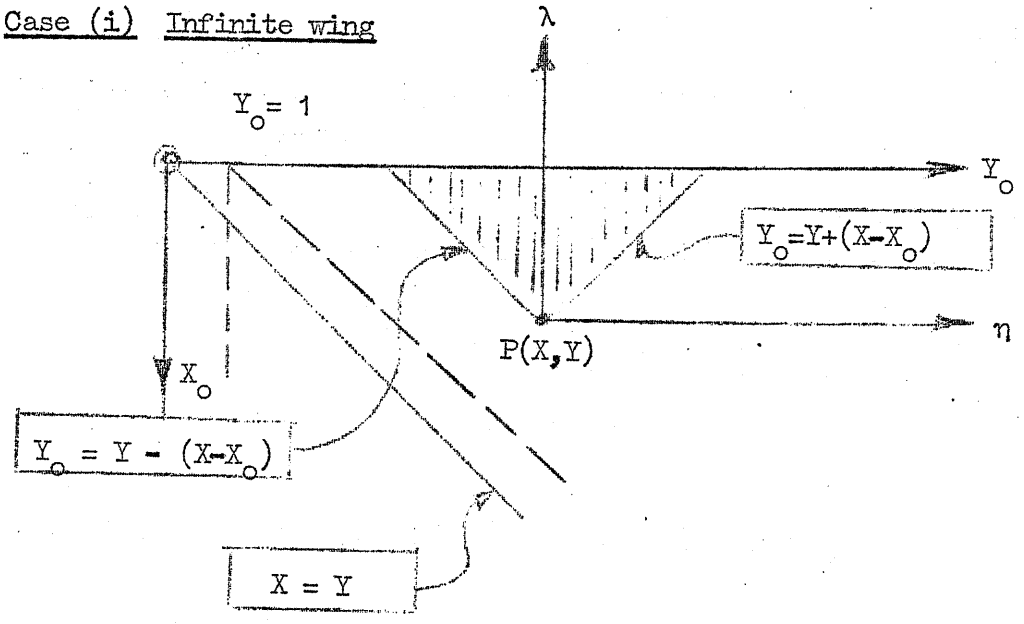

From the diagram it can be shown that

$$\frac{BC_p}{a} = \frac{\partial}{\partial X} \int_X^{\circ} d\lambda \int_{-\lambda}^{\lambda} F(\lambda,\eta)\, d\eta$$

$$= -\int_{-X}^{X} F(X,\eta)\, d\eta \quad *$$

$$= -2\left[1 + \frac{1/Y^2}{(1-X^2/Y^2)^{3/2}}\right] \qquad \text{.....(7)}$$

which is the result given by Kirkby and Robinson.

* The upper and lower limits of the integral $\eta=X$ and $\eta=-X$, respectively, are the values of η at the intersection of the forward Mach cone from P with the leading edge.

Case (ii) Finite span wing

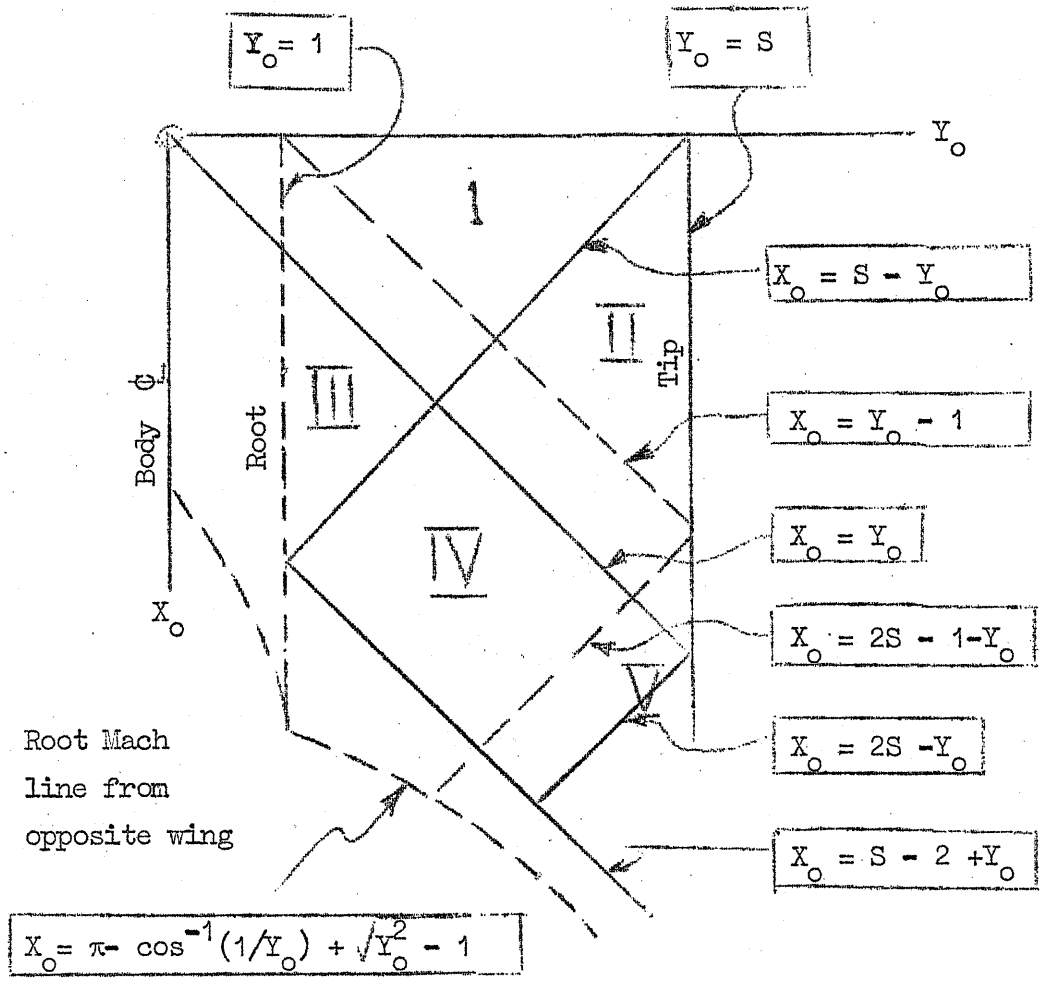

Region I $\quad X + 1 \leq Y \leq S - X$

$$\frac{BC_p}{a} = \text{Equation (7)}$$

Region II $\quad S - Y \leq X \leq Y - 1 \quad$ and $\quad Y \leq S.$

From the diagram above the appropriate limits of integration can be found for the double integration in equation (6).

Thus $$\frac{BC_p}{a} = \frac{\partial}{\partial X}\int_{S-Y}^{0} d\lambda \int_{-\lambda}^{\lambda} F(\lambda,\eta)d\eta + \frac{\partial}{\partial X}\int_{X}^{S-Y} d\lambda \int_{-\lambda}^{2(S-Y)-\lambda} F(\lambda,\eta)d\eta$$

$$= -\int_{-X}^{2(S-Y)-X} F(X,\eta)d\eta$$

$$= -\frac{4/\pi}{Y^2(1-t^2)^{3/2}}\left[\sin^{-1}\sqrt{\frac{\tau(1+t)}{1+t(2\tau-1)}} + \frac{t\sqrt{\tau(1-\tau)(1-t^2)}}{1+t(2\tau-1)}\right]$$

$$- 4/\pi \sin^{-1}\sqrt{\tau} \qquad \ldots\ldots\ldots\ldots(8)$$

where $t = X/Y$ and $\tau = \frac{S-Y}{X}$

which is the result given by Bolton-Shaw.

When $X = S-Y$, that is X lies on the tip Mach line, $\tau=1$ and equation (8) reduces to equation (7) above.

Alternatively, for the finite span wing, we can find the value of C_p which must be subtracted from the pressure coefficient for the infinite span wing.

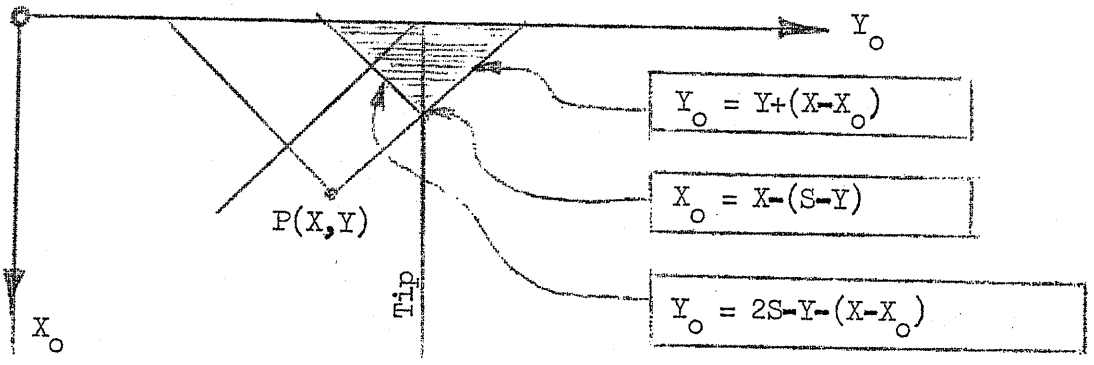

In this case, when $P(X,Y)$ is in region II, ΔC_p can be found from an integration over the shaded area in the above figure.

$$\frac{B(\Delta C_p)}{a} = \frac{\partial}{\partial X}\int_X^{S-Y} d\lambda \int_{-\lambda+2(S-Y)}^{\lambda} F(\lambda,\eta)\, d\eta$$

$$= -\int_{2(S-Y)-X}^{X} F(X,\eta)\, d\eta$$

$$= -2\left[1 + \frac{1/Y^2}{(1-t^2)^{3/2}}\right] + \frac{4}{\pi}\sin^{-1}\sqrt{\tau}$$

$$+ \frac{4/\pi}{Y^2(1-t^2)^{3/2}}\left\{\sin^{-1}\sqrt{\frac{\tau(1+t)}{1+t(2\tau-1)}} + \frac{t\sqrt{\tau(1-\tau)(1-t^2)}}{1+t(2\tau-1)}\right\}$$

.....(9)

Thus equation (7) - equation (9) = equation (8), and equation (9) can be applied when $P(X,Y)$ is in the region bounded by the tip Mach line $X_o = S-Y_o$, the tip $Y_o = S$, and the Mach line from the origin $X_o = Y_o$. When $X = Y$ it can be shown that

$$\frac{B(\Delta C_p)}{a} = \frac{4}{\pi}\sin^{-1}\sqrt{\frac{S-Y}{Y}} - 2 - \frac{(2S-Y)(2Y-S)^{\frac{1}{2}}}{3\pi Y^2(S-Y)^{3/2}} \quad ....(10)$$

When $P(X,Y)$ is downstream of the Mach line, $X_o = Y_o$, but upstream of the Mach line, $X_o = (2S-1-Y_o)$ it can be shown that the integration over the shaded area gives,

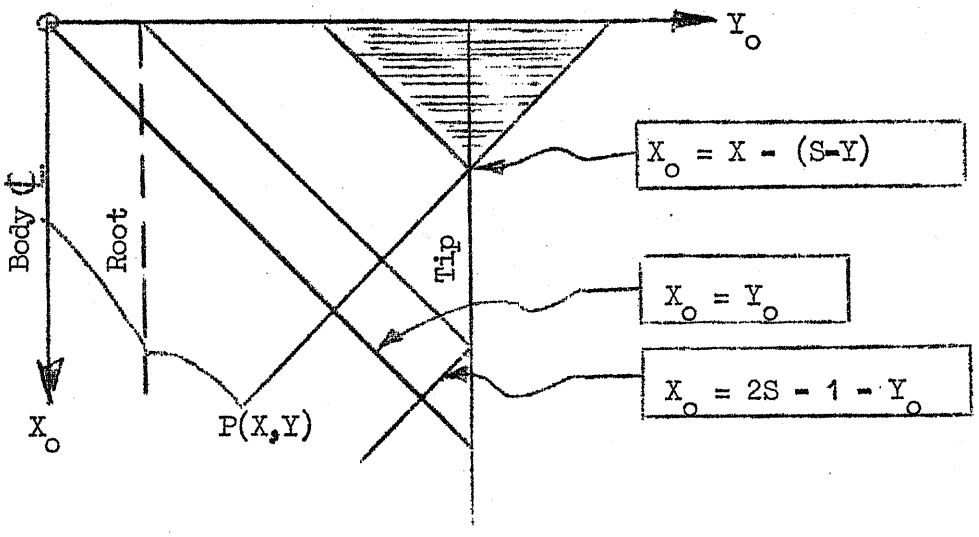

$$\frac{B(\Delta C_p)}{a} = \frac{4}{\pi} \sin^{-1}\sqrt{\tau} - 2 - \frac{4/\pi}{Y^2(t^2-1)^{3/2}} \left[\frac{t\sqrt{\tau(1-\tau)(t^2-1)}}{1 + t(2\tau-1)} + \frac{1}{2} \ln\left(\zeta - \sqrt{\zeta^2-1}\right) \right] \quad \text{.....(11)}$$

where $\zeta = \dfrac{t + 2\tau - 1}{1+t(2\tau-1)}$.

Region III

This is the region bounded by the root Mach line, $X_o = Y_o - 1$, the tip Mach line, $X_o = S - Y_o$, the root, and the root Mach line from the opposite wing,

$$X_o = \pi - \cos^{-1}\left(\frac{1}{Y_o}\right) + \sqrt{Y_o^2 - 1} \ .$$

In this region the effect of the tip is not felt and the pressure distribution is the same for a semi-infinite wing mounted on an infinitely long body.

Region IV

In this region the root Mach line from the opposite wing lies downstream of the tip Mach line reflection at the body. The region is thus bounded by the root Mach line, $X_o = Y_o - 1$, the reflected root Mach line at the tip, $X_o = 2S-1-Y_o$, the tip Mach line, $X_o = S - Y_o$, and the reflected tip Mach line, $X_o = S-2+Y_o$. The pressure distribution in this region is then found from the solution to the semi-infinite wing mounted on an infinitely long cylindrical body problem with the 'tip effect' obtained from equations (9) or (10) or (11) according as $X, <, =, >Y$.

Case (iii) Body replaced by a reflection plane at $Y_o = 1$

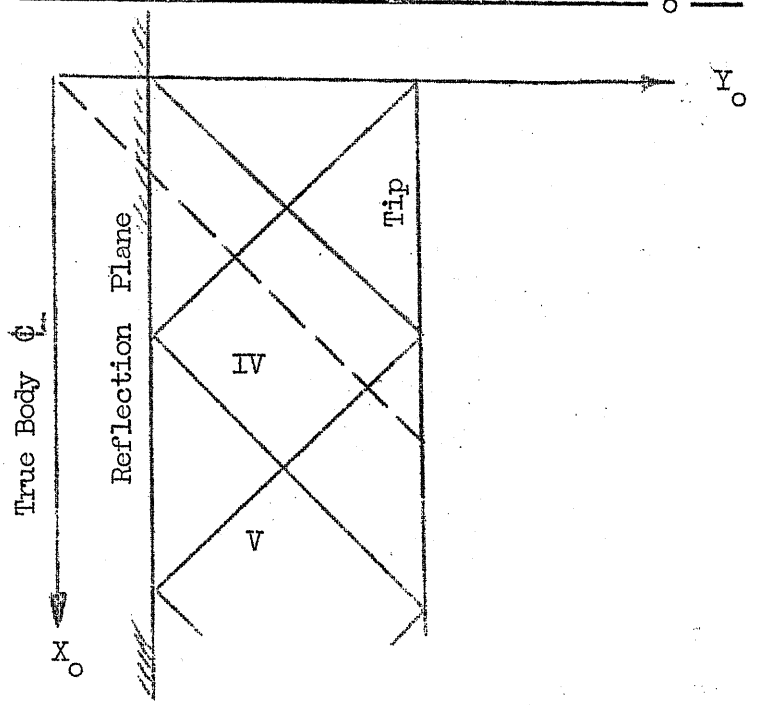

(a) P(X,Y) ahead of tip Mach line $(X_o \leq S - Y_o)$

From the above diagram the appropriate limits for the double integration in equation (6) can be determined. Thus

$$\frac{BC_p}{a} = \frac{\partial}{\partial X} \int_{Y-1}^{0} d\lambda \int_{-\lambda}^{\lambda} F(\lambda,\eta)\, d\eta$$

$$+ 2\,\frac{\partial}{\partial X} \int_{X}^{Y-1} d\lambda \int_{1-Y}^{\lambda-2(Y-1)} F(\lambda,\eta)\, d\eta$$

$$+ \frac{\partial}{\partial X} \int_{X}^{Y-1} d\lambda \int_{\lambda-2(Y-1)}^{\lambda} F(\lambda,\eta)\, d\eta$$

$$= -2 \int_{1-Y}^{X-2(Y-1)} F(X,\eta)\, d\eta - \int_{X-2(Y-1)}^{X} F(X,\eta)\, d\eta$$

$$= -\int_{1-Y}^{X} F(X,\eta)\, d\eta - \int_{1-Y}^{X-2(Y-1)} F(X,\eta)\, d\eta$$

(i) ...

(i) For $(1 - 1/Y) < t < 1$

$$\frac{BC_p}{a} = \frac{4}{\pi Y(1-t^2)}\left[\sqrt{t^2 - \left(1 - \frac{1}{Y}\right)^2} - \frac{\sqrt{(1-1/Y)(t-1+1/Y)}}{Y\left(t + \frac{2}{Y} - 1\right)}\right]$$

$$- \frac{4}{\pi Y^2(1-t^2)^{3/2}}\left[2 \sin^{-1}\sqrt{\frac{(1-t)(t+1-1/Y)}{2\,t/Y}}\right.$$

$$\left. - \sin^{-1}\sqrt{\frac{(1-t)(1-1/Y)}{t(t-1+2/Y)}}\right]$$

$$- \frac{8}{\pi}\sin^{-1}\sqrt{\frac{t+1-1/Y}{2t}} + \frac{4}{\pi}\sin^{-1}\sqrt{\frac{1-1/Y}{t}} \quad \ldots\ldots\ldots(12)$$

(ii) For $t = 1$

$$\frac{BC_p}{a} = \frac{(1+2/Y)}{3\pi}\sqrt{\frac{1}{Y}\left(1 - \frac{1}{Y}\right)} - \frac{4}{3\pi}\left(1 + \frac{1}{Y}\right)\sqrt{\frac{2}{Y} - \frac{1}{Y^2}}$$

$$- \frac{8}{\pi}\sin^{-1}\sqrt{\frac{2 - 1/Y}{2}} + \frac{4}{\pi}\sin^{-1}\sqrt{1 - 1/Y}$$

$\ldots\ldots\ldots\ldots(13)$

(iii) When $t > 1$

$$\frac{BC_p}{a} = -\frac{4}{\pi Y(t^2-1)}\left[\sqrt{t^2-(1-1/Y)^2} - \frac{\sqrt{(1-1/Y)(t-1+1/Y)}}{Y\left(t + \frac{2}{Y} - 1\right)}\right]$$

$$- \frac{2}{\pi Y^2(t^2-1)^{3/2}}\left[2\, l_n\left\{\frac{(t^2-1+1/Y) - \sqrt{(t^2-1)\left[t^2-(1-1/Y)^2\right]}}{t/Y}\right\}\right.$$

$$\left. - l_n\left\{\frac{t^2+t-2+2/Y - \sqrt{(t^2-1)\left[t^2-(t-2+2/Y)^2\right]}}{t(t-1+2/Y)}\right\}\right]$$

$$- \frac{8}{\pi}\sin^{-1}\sqrt{\frac{t+1-1/Y}{2t}} + \frac{4}{\pi}\sin^{-1}\sqrt{\frac{1 - 1/Y}{t}} \quad \ldots\ldots(14)$$

(b) P(X,Y) in region IV

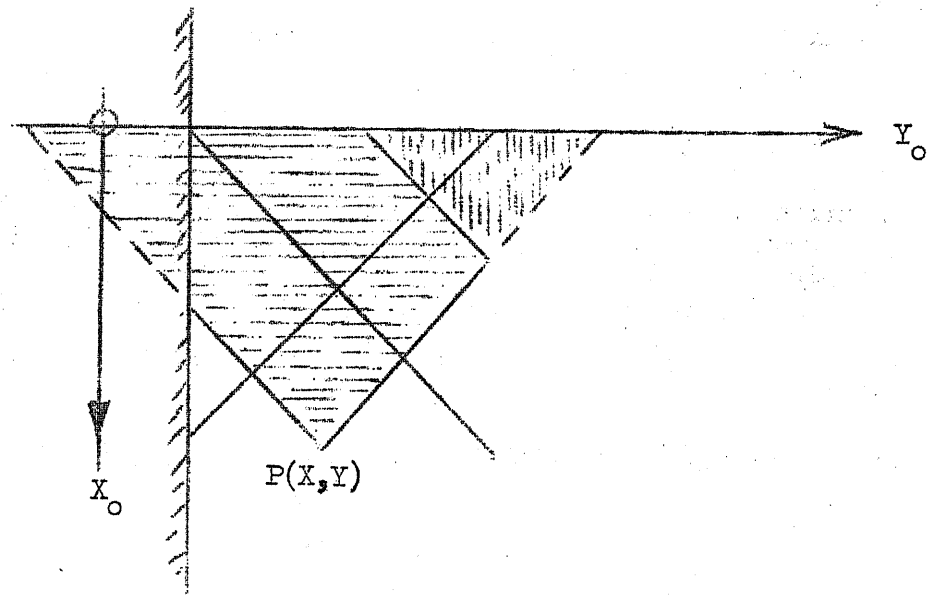

The value of $\frac{BC_p}{a}$ in this region can be obtained from an integration of $F(\lambda,\eta)$ over the area shaded (≡).

Alternatively $\frac{BC_p}{a}$ can be obtained from the expressions given in one of equations (12) to (14) from which is subtracted the integration over the 'tip correction area' shaded (|||) above. If P(X,Y) is upstream of the reflected root Mach line, $X_o = (2S-1-Y_o)$, the correction to BC_p/a can be found from one of the equations (9) to (11).

(c) P(X,Y) in region V

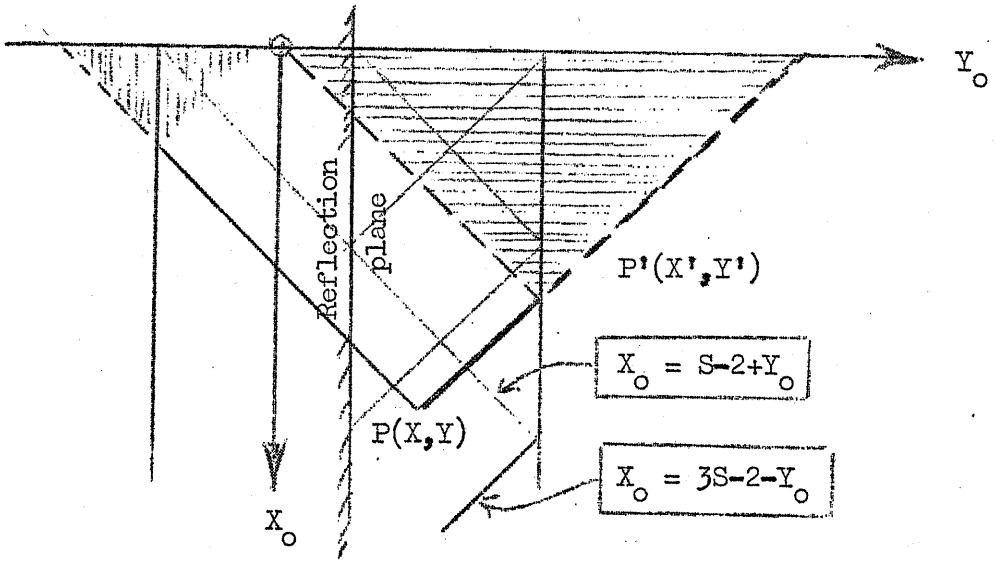

When $P(X,Y)$ is downstream of the reflected root Mach line, $X_o = 2S-1-Y_o$, the value of BC_p/a can be found from one of equations (12) to (14) from which is subtracted the appropriate tip correction.

When $P(X,Y)$ is upstream of the reflected tip Mach line, $X_o = 3S-2-Y_o$, and downstream of the Mach line, $X_o = S-2+Y_o$, a tip correction for both the tip and its image must be applied. When $P(X,Y)$ is upstream of the Mach line, $X_o = S-2+Y_o$, the image tip correction is zero. When $P'(X',Y')$ falls downstream of the reflected tip Mach line, $X_o = 3S-2-Y_o$ a different procedure must be adopted,[3] in order to satisfy the boundary condition that $\phi = 0$ beyond the tip.

(d) <u>The chordwise pressure distribution along the reflection plane $Y_o = 1$</u>

$X = 0$

$$\frac{BC_p}{a} = -4 \qquad \text{.....(15)}$$

$0 < X < 1$

$$\frac{BC_p}{a} = \frac{4t}{\pi(1-t^2)} - \frac{8}{\pi}\,\frac{\sin^{-1}\sqrt{\frac{1-t}{2}}}{(1-t^2)^{3/2}} - 2 \qquad \text{.....(16)}$$

$X = 1$

$$\frac{BC_p}{a} = -2 - \frac{8}{3\pi} \qquad \text{.....(17)}$$

$1 < X < (S-1)$

$$\frac{BC_p}{a} = -\frac{4t}{\pi(t^2-1)} - \frac{4}{\pi}\,\frac{l_n\left(t-\sqrt{t^2-1}\right)}{(t^2-1)^{3/2}} - 2 \qquad \text{.....(18)}$$

$(S-1) < X < (2S-1)$

$$\frac{BC_p}{a} = (18) - \frac{4}{\pi}\sin^{-1}\sqrt{\tau} + 2 + \frac{4}{\pi(t^2-1)^{3/2}}\left[\frac{t\sqrt{(t^2-1)\tau(1-\tau)}}{1+t(2\tau-1)} + \frac{1}{2}\,l_n\left(\zeta-\sqrt{\zeta^2-1}\right)\right] \qquad \text{.....(19)}$$

where $t = X$; $\tau = \dfrac{S-1}{t}$

$$\zeta = \frac{t+2\tau-1}{1+t(2\tau-1)} \,.$$

These results are plotted in figure 86.

TABLE I

Mean chordwise and spanwise positions of holes

Chordwise stations

Hole No.	x/c
I	0.014
II	0.041
III	0.116
1	0.161
2	0.207
3	0.250
4	0.298
5	0.340
6	0.435
7	0.477
8	0.516
9	0.569
10	0.606
11	0.659
12	0.701
13	0.745
14	0.791
15	0.885
16	0.926
17	0.968

Spanwise stations

Col. No.	y/s	y/a
1	0.918	2.494
2	0.792	2.152
3	0.714	1.940
4	0.598	1.625
5	0.525	1.427
6	0.400	1.087
tip holes	0.901	2.450
centre '	0.684	1.860
root '	0.480	1.305

c = chord
s = span
a = body radius
x = chordwise coordinate
y = spanwise coordinate

11. References

1. Busing, J.R., and Lilley, G.M. — A preliminary investigation of the flow over a particular wing-body combination at M = 2.0. College of Aeronautics Tech. Note No. 24, (1955).

2. Lawrence, H.R., and Flax, A.H. — Wing body interference at subsonic and supersonic speeds - survey and new developments. J.Ae.Sc., 289, 21, May, 1954.

3. Gunn, J.C. — Linearised supersonic aerofoil theory. Phil.Trans.Roy.Soc. (Series A), 327, 240, 1946-8.

4. Beskin, L. — Determination of upwash around a body of revolution at supersonic velocities. Consolidated-Vultee Aircraft Corporation Bumble bee report No. CM.251, May, 1946.

5. Kirkby, S., and Robinson, A. — Wing body interference at supersonic speeds. College of Aeronautics Report No. 7, April, 1947.

6. Bolton-Shaw, B.W. — The lifting-pressure distribution on a finite wing with a supersonic leading edge due to the upwash field of a body. English Electric Report No. LA.t.035, June, 1952.

7. Ferrari, C. — Interference between wing and body at supersonic speeds. Theory and numerical applications. J.Ae.Sc., 317, 15, June 1948.

8. Morikawa, G.K. — The wing-body problem for linearised supersonic flow. Cal. Tech. Doctoral Thesis, 1949.

   A non-planar boundary problem for the wave equation. Qu.App.Maths.,129, 10, July, 1952.

9. Nielsen, J.N. — Supersonic wing-body interference. Cal.Tech.Doctoral Thesis, 1951.
   Wing body interference at supersonic speeds with applications to combinations with rectangular wings. N.A.C.A. T.N. 2677, 1952.

References (Contd.)

10. Chester, W. — Supersonic flow past wing-body combinations. Aeronautical Quarterly, Part 3, Vol. 4, August, 1953.

11. Ward, G.N. — Supersonic flow past slender pointed bodies. Quar.Jnl. of Mechs. and App. Maths. Part I. 76, II, 1949.

12. Browne, S.H., Friedman, L., and Hodes, I. — A wing-body problem in a supersonic conical flow. J.Ae.Sc., 443, 15, August 1948.

13. Nielsen, J.N., and Kaattari, G.E. — Method for estimating lift interference of wing-body combinations at supersonic speeds. N.A.C.A. R.M. A51J04, December, 1951.

14. Flax, A.H., and Lawrence, H.R. — The aerodynamics of low aspect ratio wings and wing-body combinations. Third Anglo-American Aeronautical Conference, 1951.

15. Spreiter, J.R. — Aerodynamic properties of slender wing-body combinations at subsonic, transonic and supersonic speeds. N.A.C.A. T.N. 1662, July 1948.

16. Warren, C.H.E. — Definitions of angles of incidence and sideslip. A.R.C. Current Paper 124, 1953.

17. Nielsen, J.N., and Pitts, W.C. — Wing body interference at supersonic speeds with an application to combinations with rectangular wings. N.A.C.A. T.N. 2677, April, 1952.

18. Pitts, W.C., Nielsen, J.N., and Gionfridds, M.P. — Comparison between theory and experiment for interference pressure field between wing and body at supersonic speeds. N.A.C.A. T.N. 3128, April, 1954.

19. Evvard, J.C. — Use of source distributions for evaluating theoretical aerodynamics of thin finite wings at supersonic speeds. N.A.C.A. Report No. 951, 1950.

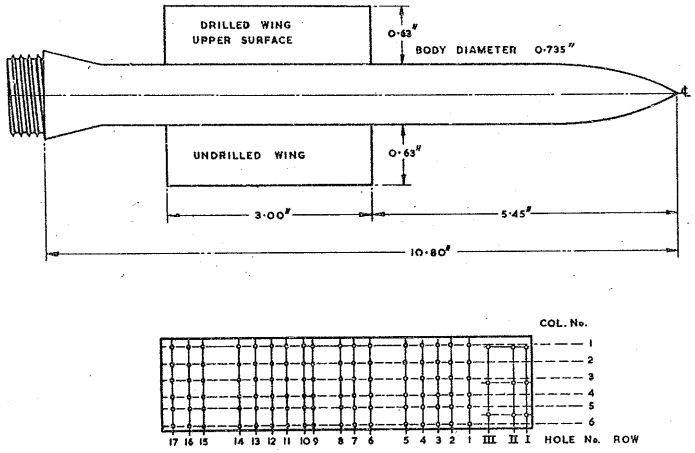

FIG. 1. DIMENSIONS OF MODEL AND POSITIONS OF PRESSURE TAPPINGS.

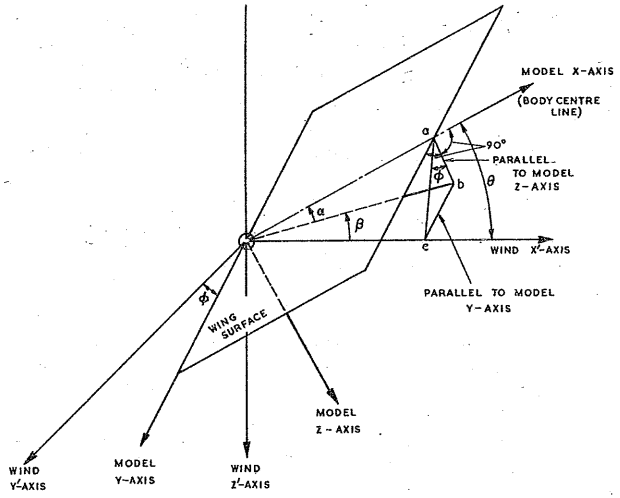

$$\tan \alpha = \frac{ab}{Oa} = \frac{ab}{ac}\,\frac{ac}{Oa} = \cos \phi \tan \theta$$

$$\sin \beta = \frac{bc}{Oc} = \frac{bc}{ac}\,\frac{ac}{Oc} = \sin \phi \sin \theta$$

FIG. 2. ORIENTATION OF MODEL IN WIND TUNNEL

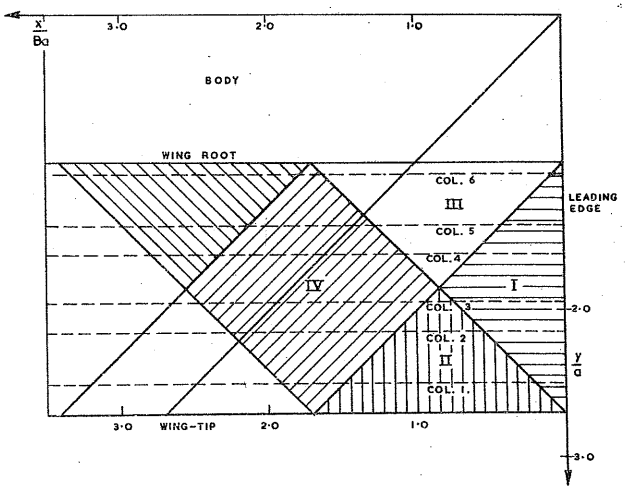

FIG. 3. POSITIONS OF MACH WAVES ON WING.

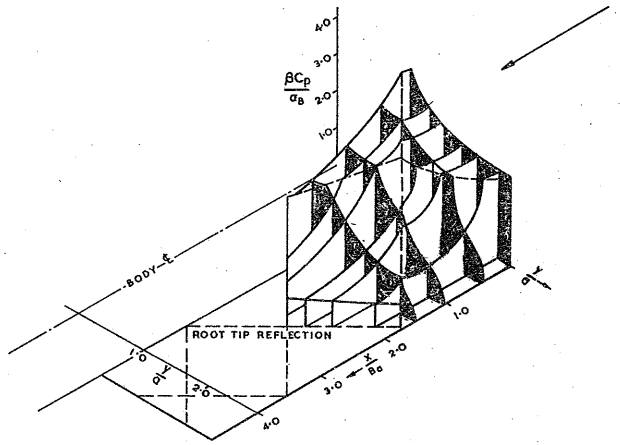

FIG. 4. MORIKAWAS SOLUTION WITH TIP CORRECTIONS APPLIED.

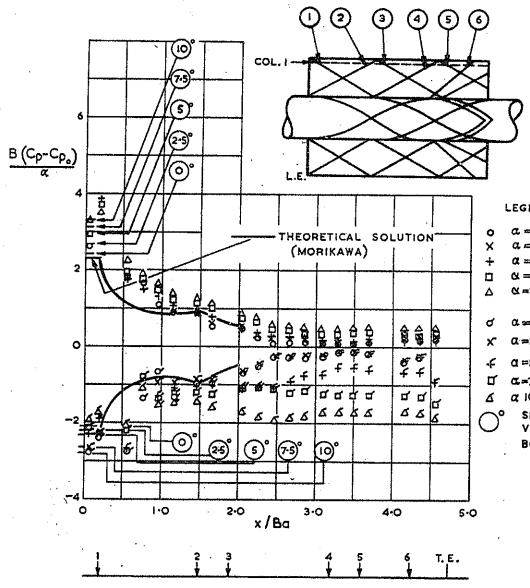

FIG. 5. CHORDWISE PRESSURE DISTRIBUTION ON WING AT 0° ROLL. y/a=2·49 (Col. 1)

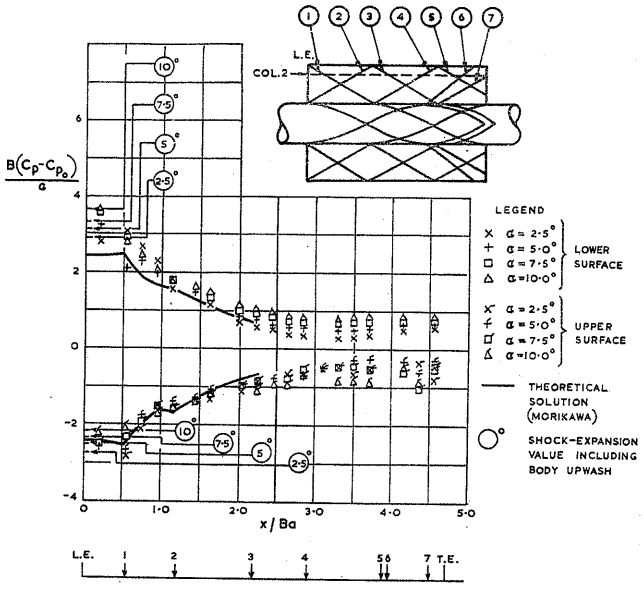

FIG. 6. CHORDWISE PRESSURE DISTRIBUTION ON WING AT 0° ROLL. y/a=2·15 (Col. 2)

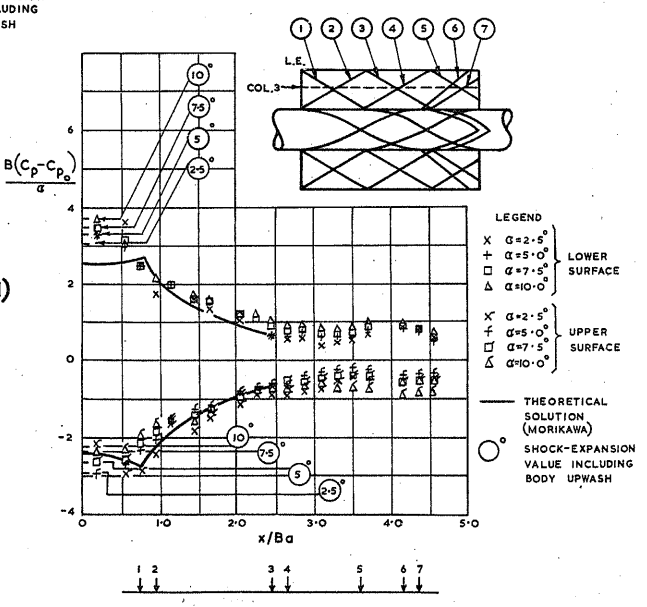

FIG. 7. CHORDWISE PRESSURE DISTRIBUTION ON WING AT 0° ROLL. y/a=1·94 (Col. 3)

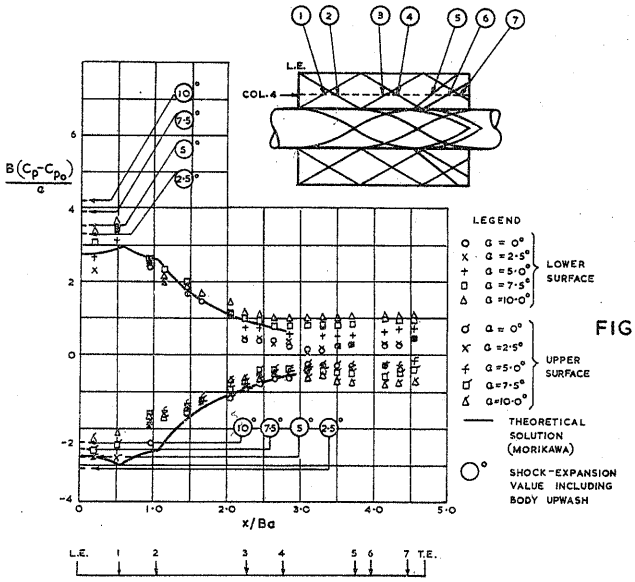

FIG. 8. CHORDWISE PRESSURE DISTRIBUTION ON WING AT 0° ROLL. y/a=1·625(Col.4)

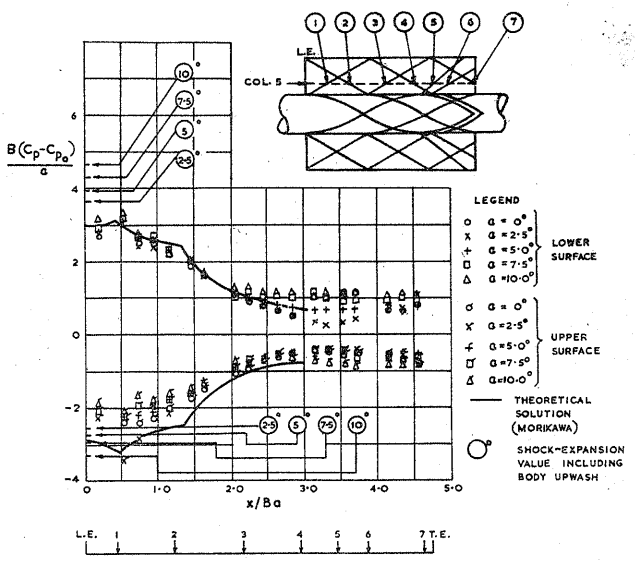

FIG. 9. CHORDWISE PRESSURE DISTRIBUTION ON WING AT 0° ROLL. y/a=1·425(Col. 5)

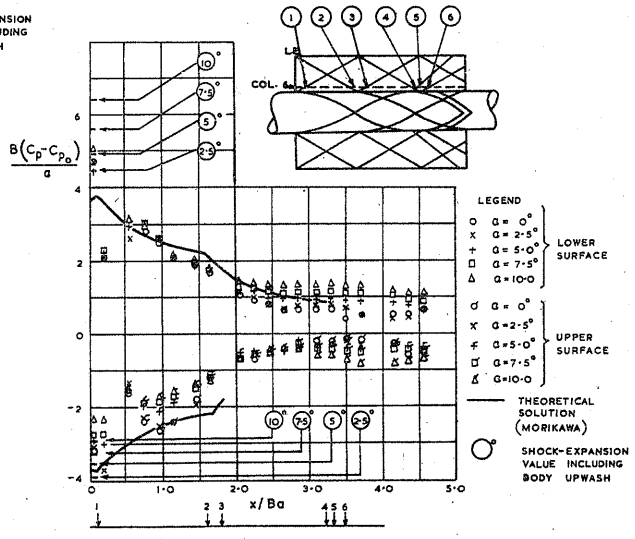

FIG. 10. CHORDWISE PRESSURE DISTRIBUTION ON WING AT 0° ROLL. y/a=1·09(Col. 6)

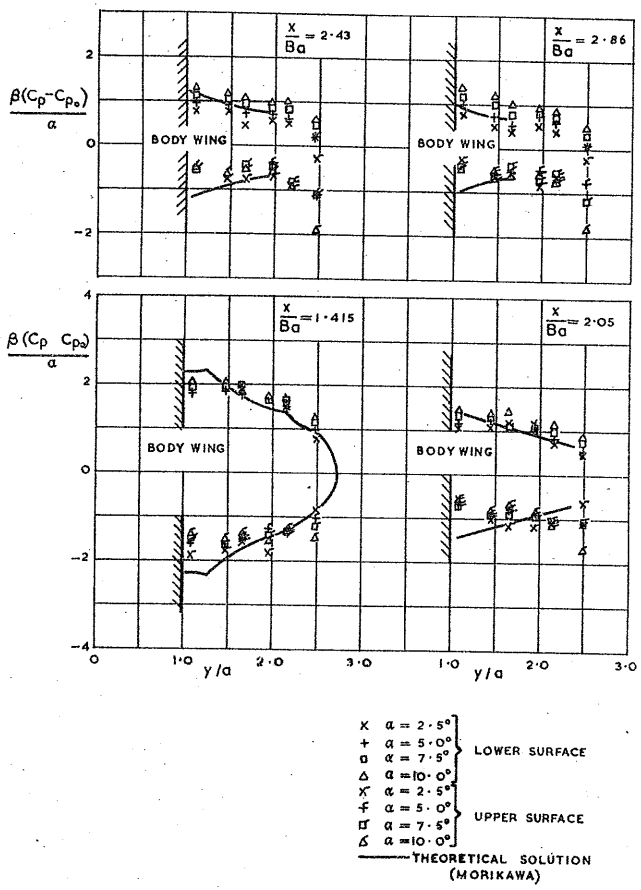

FIG 11 cont. SPANWISE PRESSURE DISTRIBUTION ON WING AT 0° ROLL

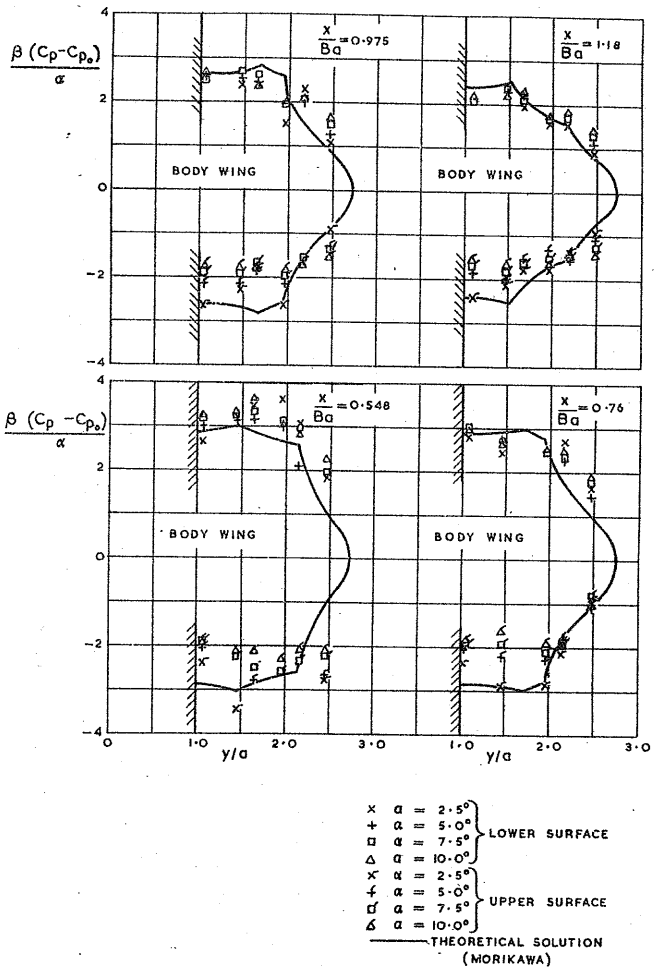

FIG.11. SPANWISE PRESSURE DISTRIBUTION ON WING AT 0° ROLL

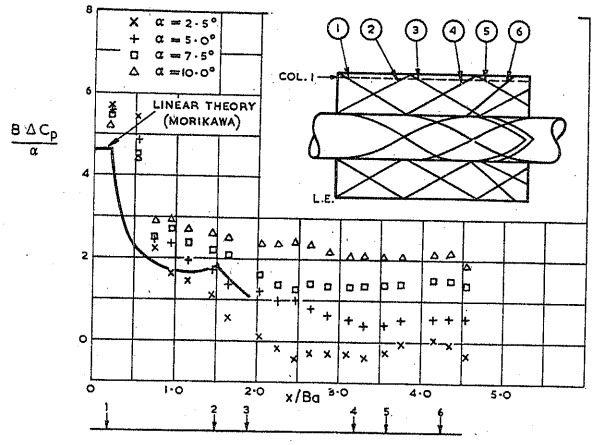

FIG. 12. CHORDWISE DISTRIBUTION OF NORMAL FORCE AT 0° ROLL. y/a = 2 49 (Col. 1)

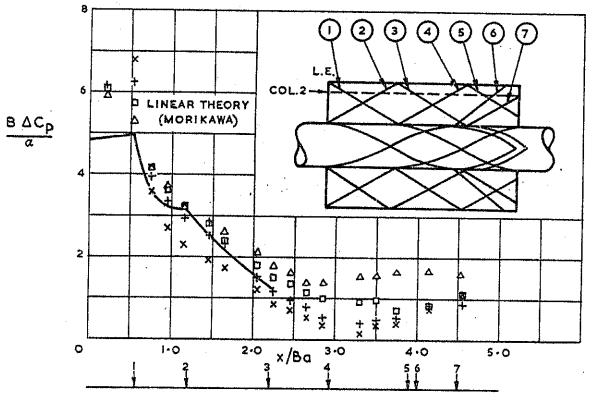

FIG. 13. CHORDWISE DISTRIBUTION OF NORMAL FORCE AT 0° ROLL. y/a = 2·15 (Col. 2)

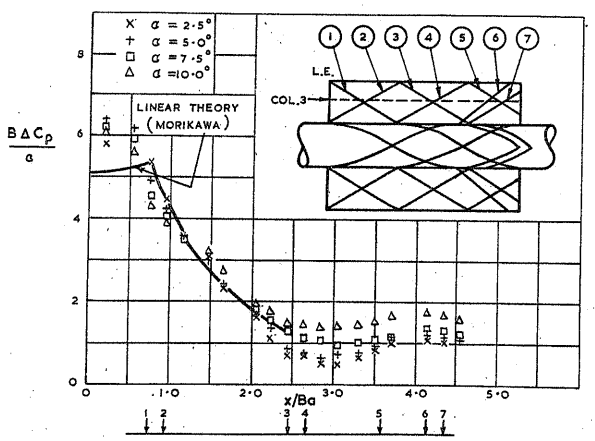

FIG. 14. CHORDWISE DISTRIBUTION OF NORMAL FORCE AT 0° ROLL. y/a = 1·94 (Col. 3)

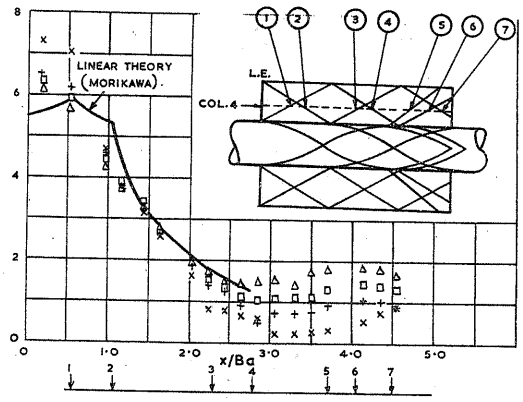

FIG. 15. CHORDWISE DISTRIBUTION OF NORMAL FORCE AT 0° ROLL. y/a = 1·625 (Col. 4)

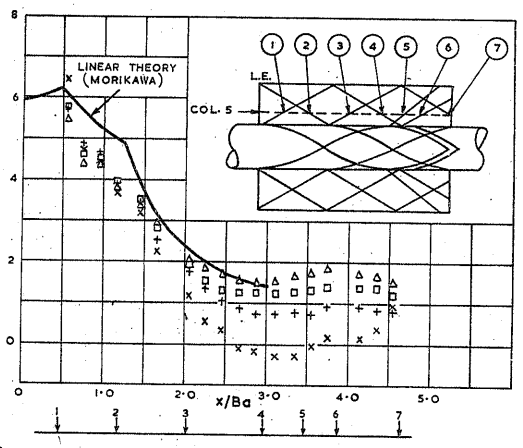

FIG. 16. CHORDWISE DISTRIBUTION OF NORMAL FORCE AT 0° ROLL. y/a = 1·49 (Col. 5)

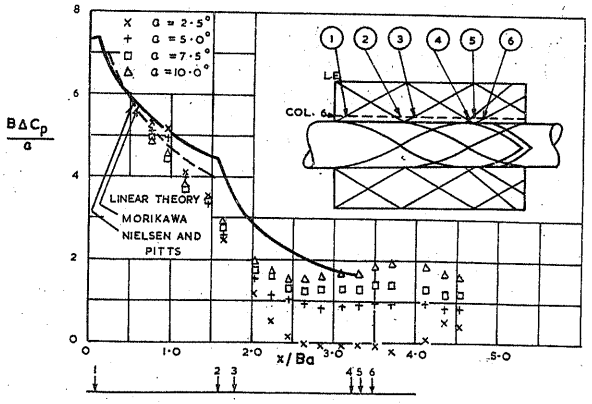

FIG. 17. CHORDWISE DISTRIBUTION OF NORMAL FORCE AT 0° ROLL. y/a = 1·09 (Col. 6)

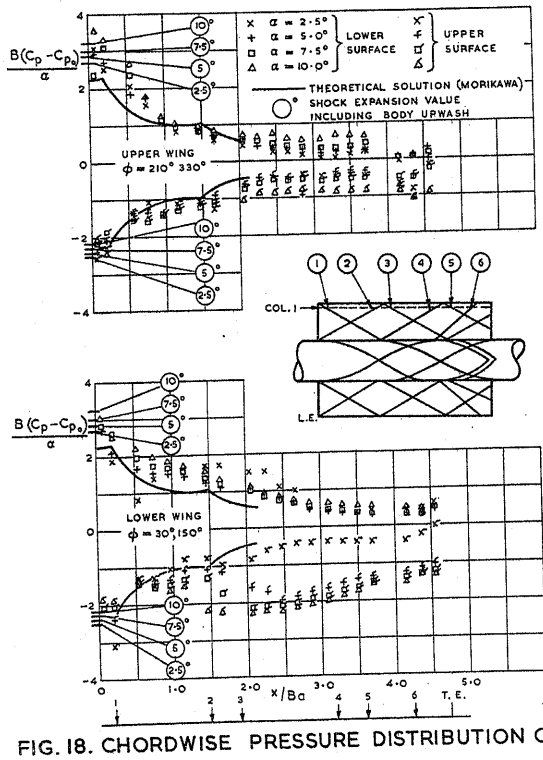

FIG. 18. CHORDWISE PRESSURE DISTRIBUTION ON WINGS AT 30° ROLL y/a = 2·49 (Col.1)

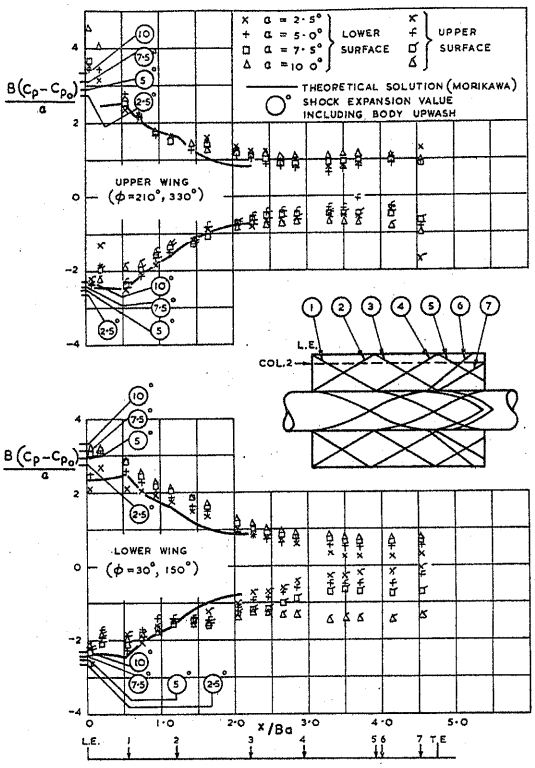

FIG. 19. CHORDWISE PRESSURE DISTRIBUTION ON WINGS AT 30° ROLL. y/a = 2·15 (Col.2)

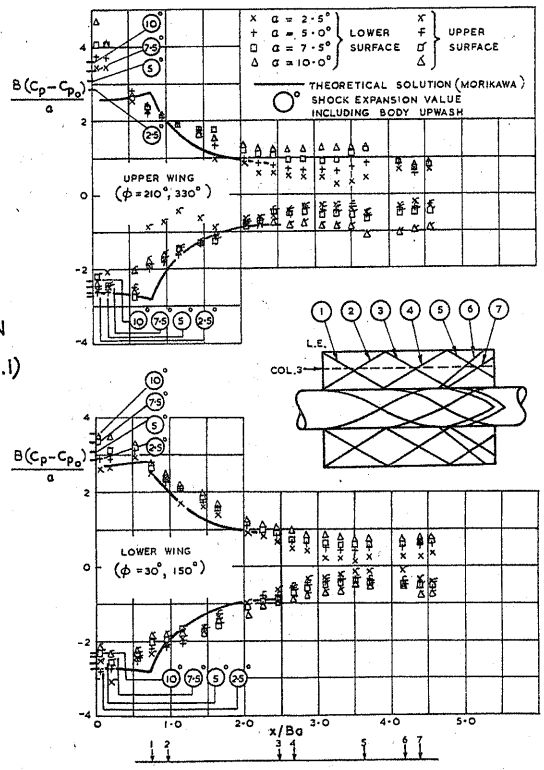

FIG. 20. CHORDWISE PRESSURE DISTRIBUTION ON WINGS AT 30° ROLL. y/a = 1·94 (Col.3)

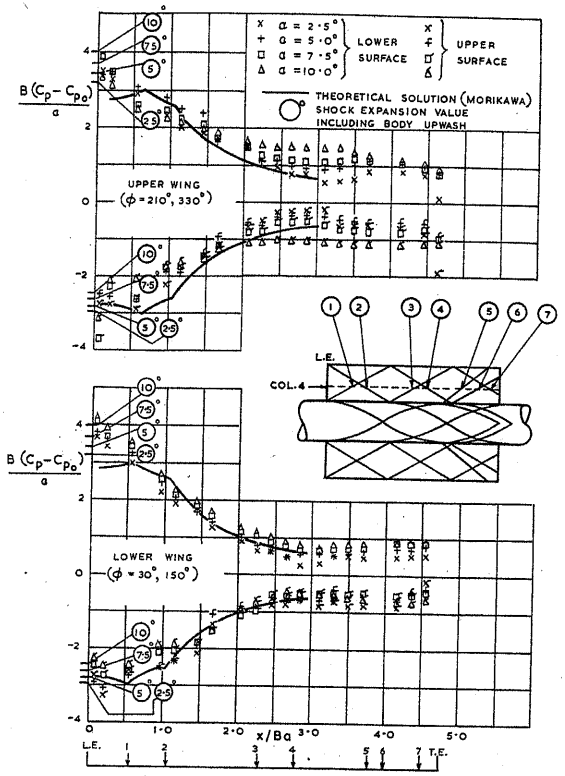

FIG. 21. CHORDWISE PRESSURE DISTRIBUTION ON WINGS AT 30° ROLL. y/a=1·625(Col.4)

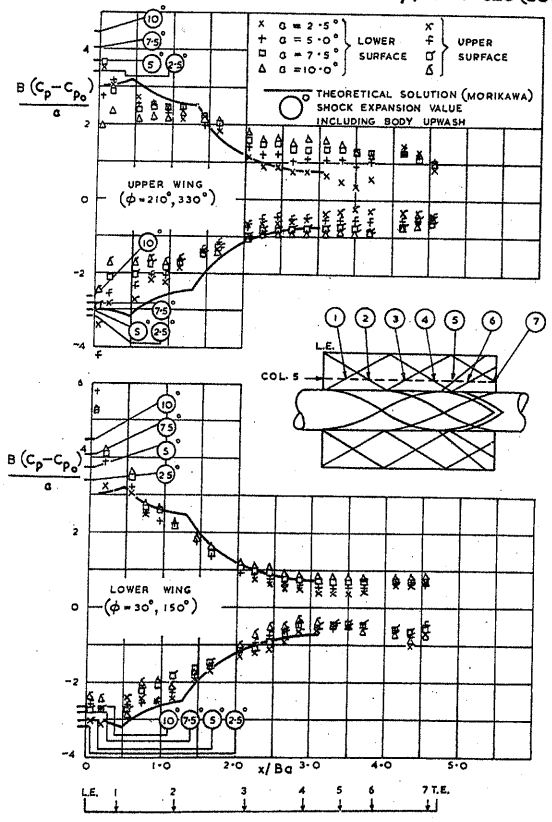

FIG. 22. CHORDWISE PRESSURE DISTRIBUTION ON WINGS AT 30° ROLL. y/a=1·43 (Col.5)

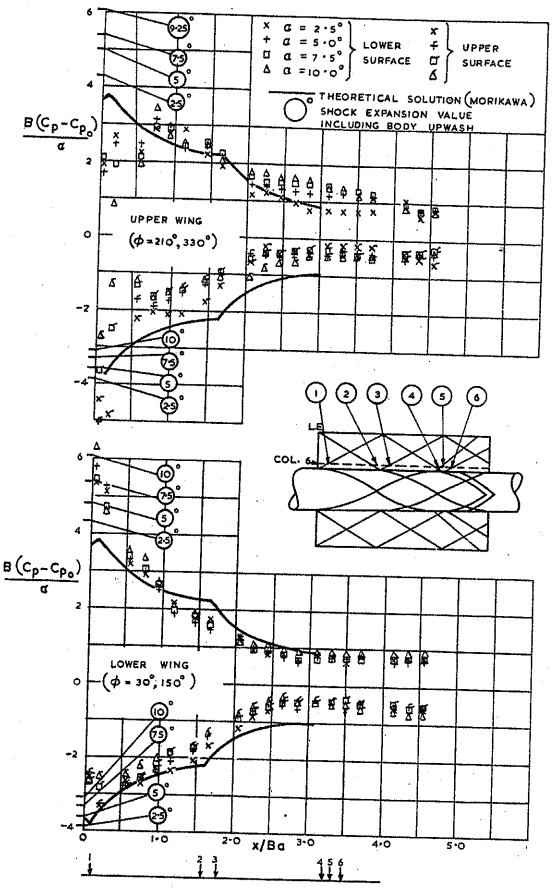

FIG. 23. CHORDWISE PRESSURE DISTRIBUTION ON WINGS AT 30° ROLL. y/a=1·09 (Col.6)

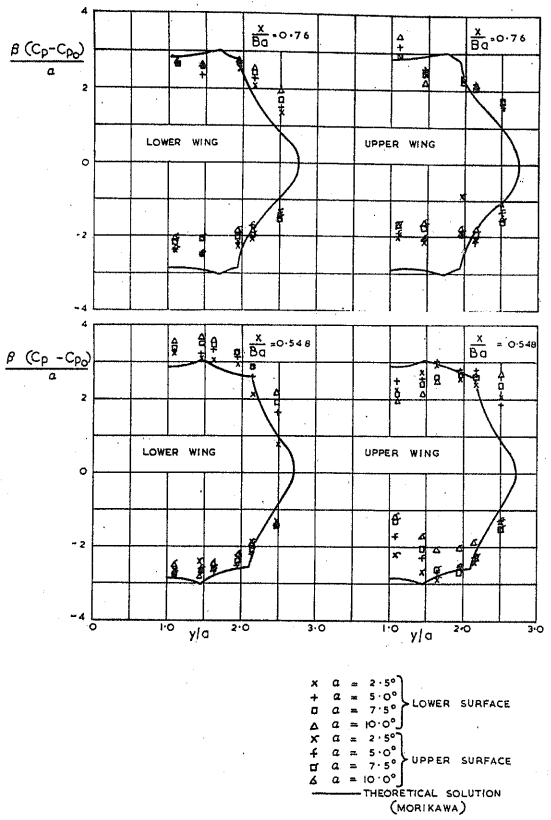

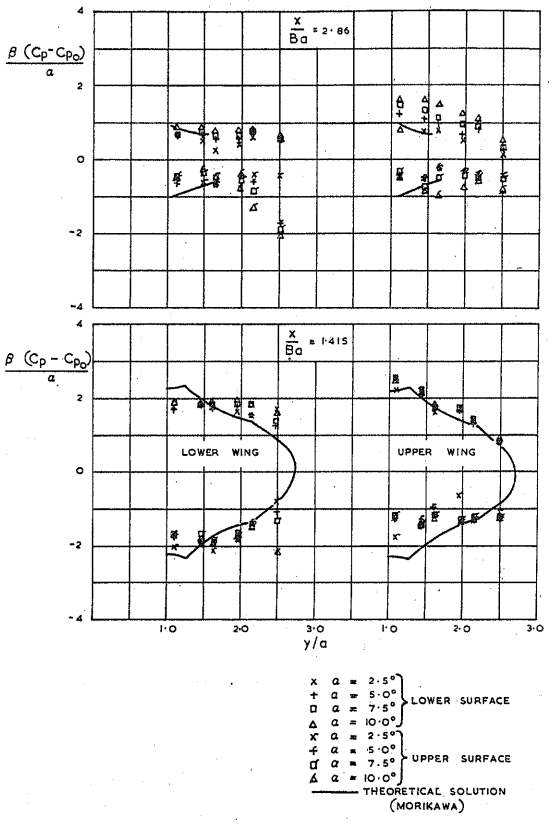

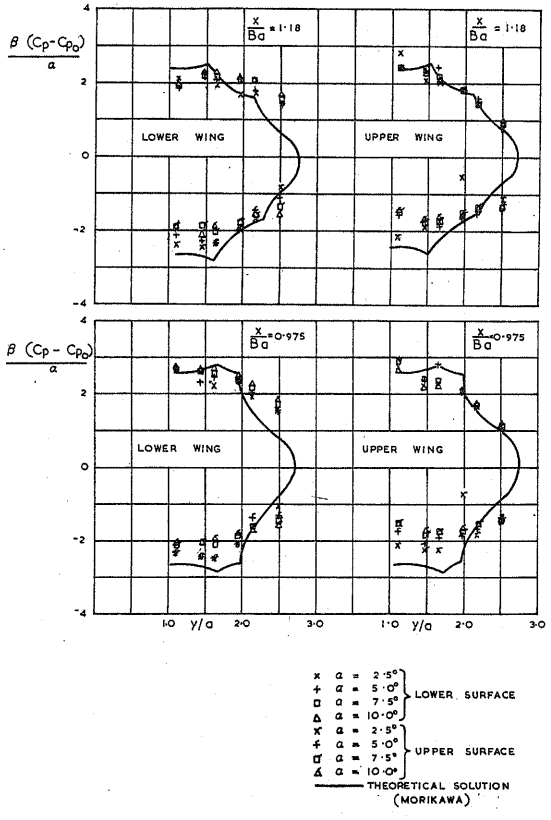

SPANWISE PRESSURE DISTRIBUTION ON WINGS AT 30° ROLL

FIG.24.

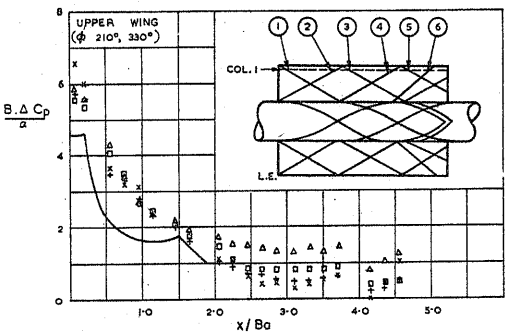

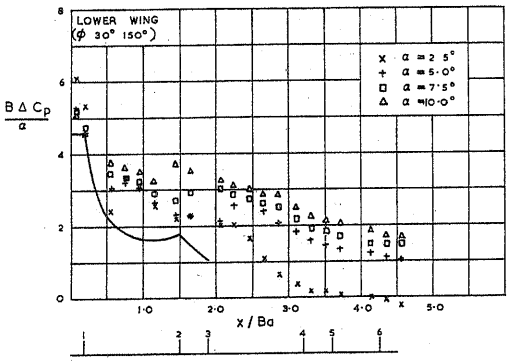

FIG. 25. CHORDWISE DISTRIBUTION OF NORMAL FORCE AT 30° ROLL. y/a=2·49 (Col. 1)

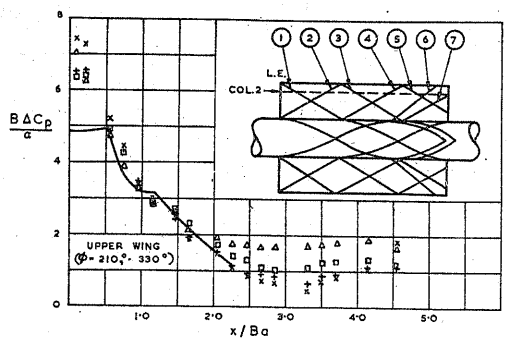

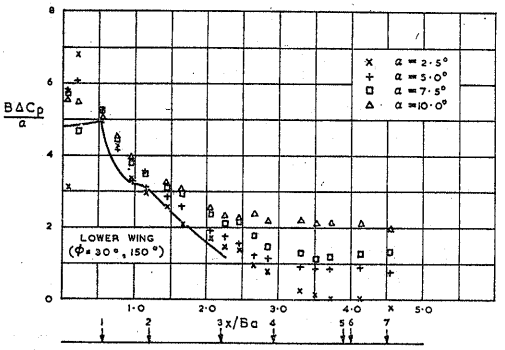

FIG.26 CHORDWISE DISTRIBUTION OF NORMAL FORCE AT 30° ROLL y/a = 2 15 (Col. 2)

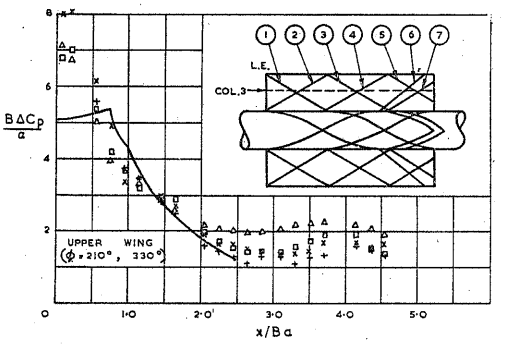

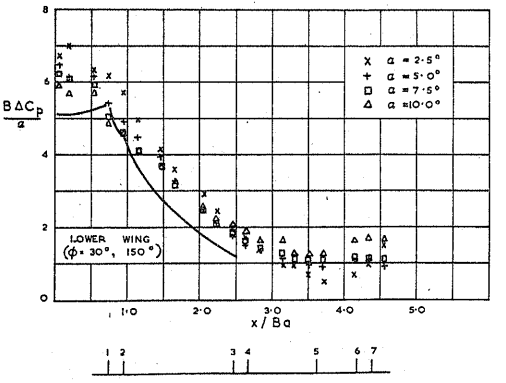

FIG. 27. CHORDWISE DISTRIBUTION OF NORMAL FORCE AT 30° ROLL. y/a 1·94 (Col. 3)

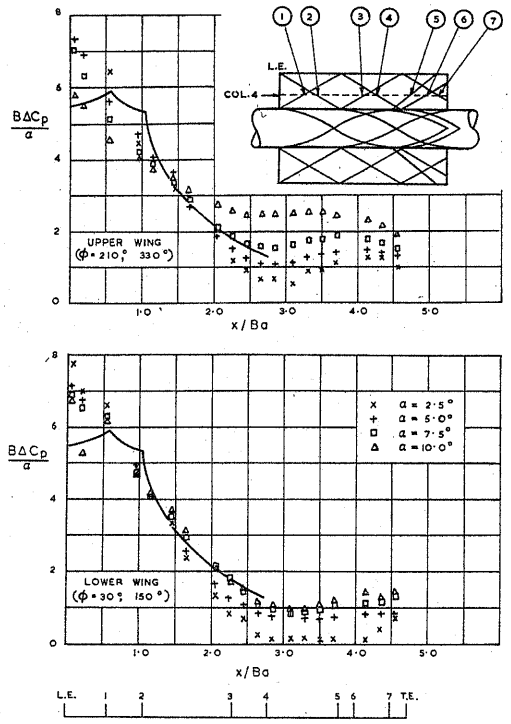

FIG. 28. CHORDWISE DISTRIBUTION OF NORMAL FORCE AT 30° ROLL y/a = 1·625 (Col. 4)

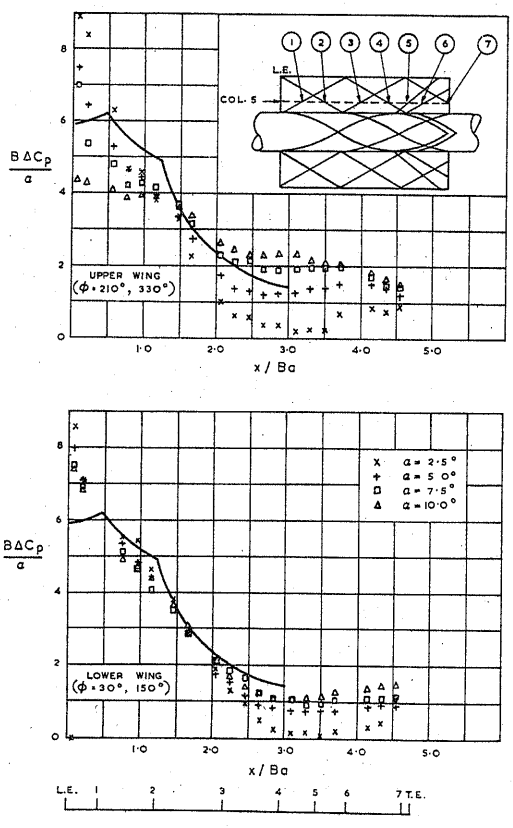

FIG. 29. CHORDWISE DISTRIBUTION OF NORMAL FORCE AT 30° ROLL y/a = 1·625 (Col. 5)

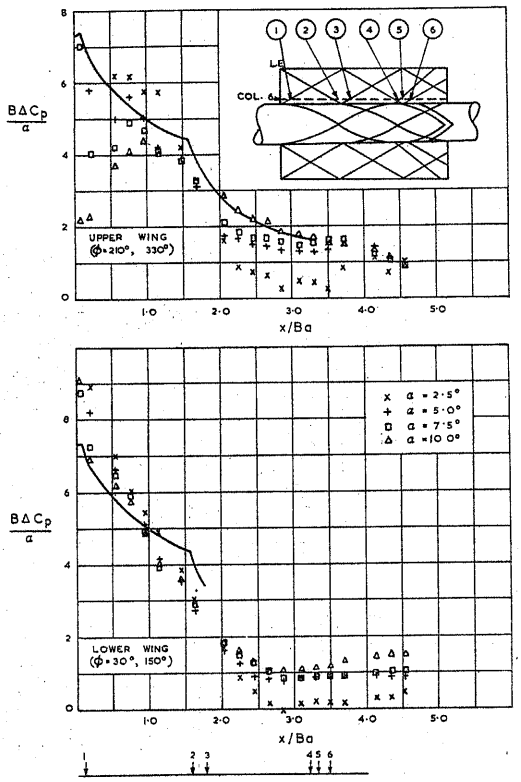

FIG. 30. CHORDWISE DISTRIBUTION OF NORMAL FORCE AT 30° ROLL. y/a = 1·09 (Col. 6)

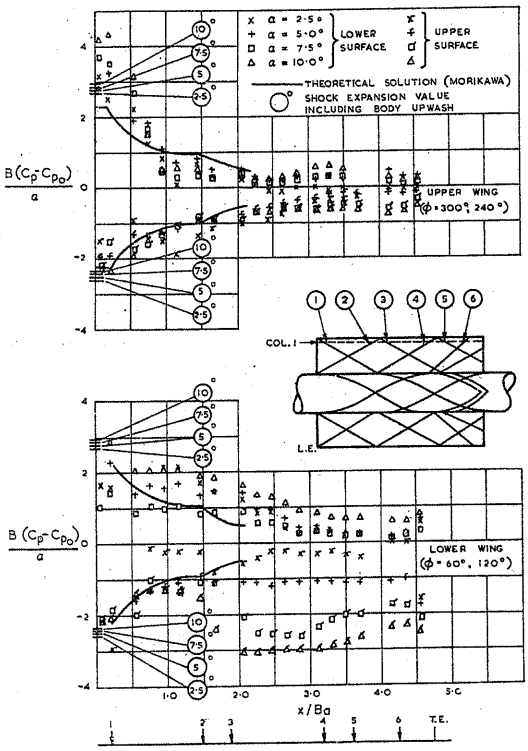

FIG. 31. CHORDWISE PRESSURE DISTRIBUTION ON WINGS AT 60° ROLL. y/a = 2·49 (Col.1)

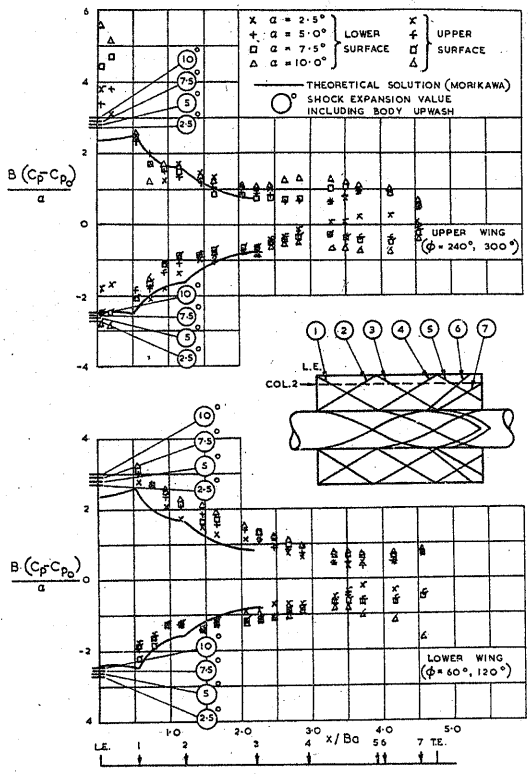

FIG. 32. CHORDWISE PRESSURE DISTRIBUTION ON WINGS AT 60° ROLL. y/a = 2·15 (Col.2)

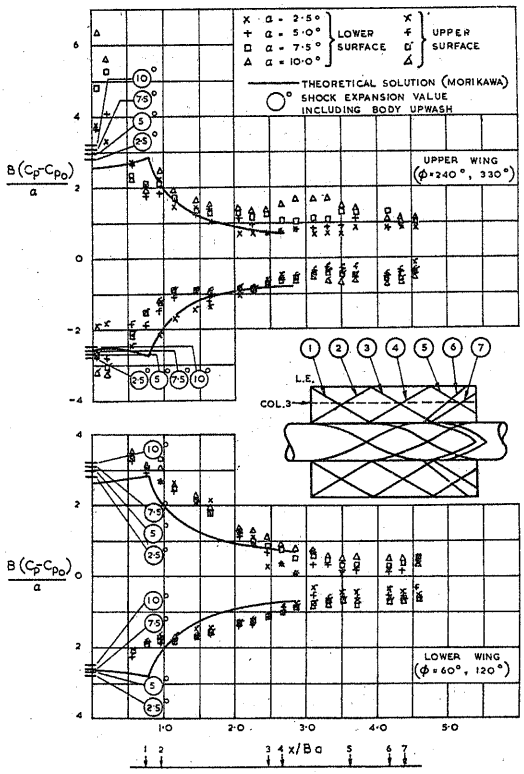

FIG. 33. CHORDWISE PRESSURE DISTRIBUTION ON WINGS AT 60° ROLL. y/a 1·94 (Col.3)

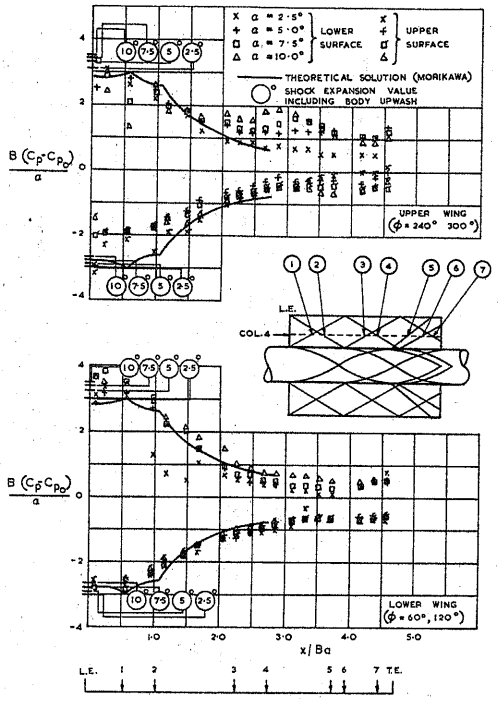

FIG. 34. CHORDWISE PRESSURE DISTRIBUTION ON WINGS AT 60° ROLL. y/a = 1·625 (Col. 4)

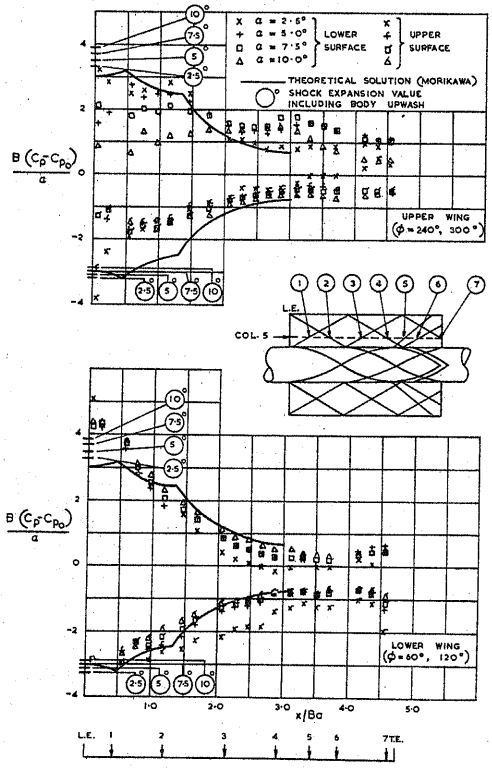

FIG. 35. CHORDWISE PRESSURE DISTRIBUTION ON WINGS AT 60° ROLL. y/a = 1·43 (Col. 5)

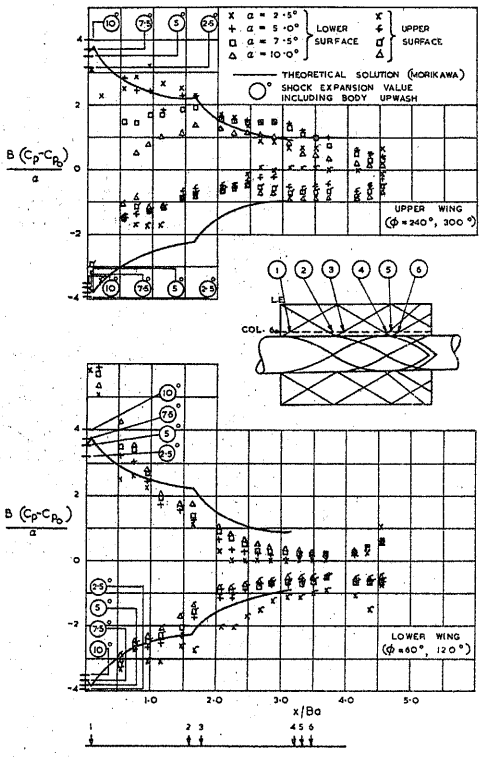

FIG. 36 CHORDWISE PRESSURE DISTRIBUTION ON WINGS AT 60° ROLL. y/a = 1·09 (Col. 6.)

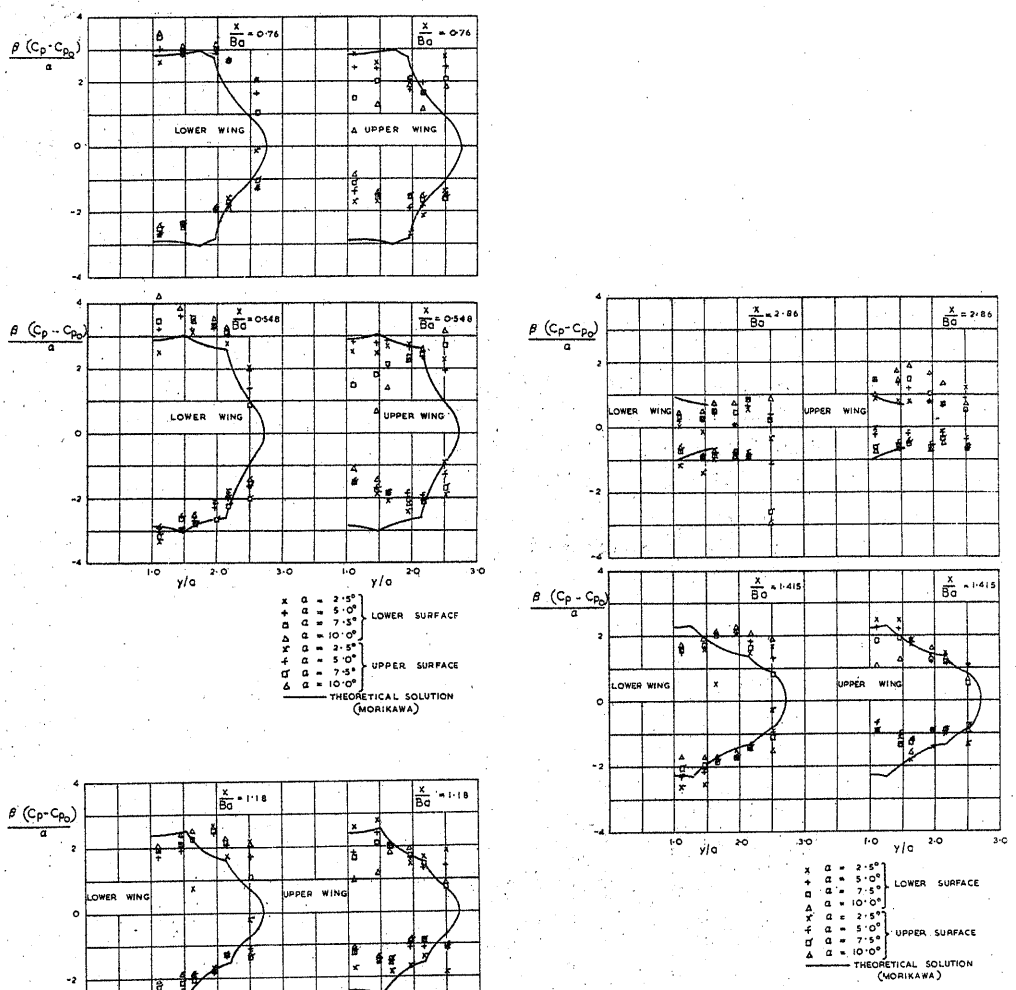

SPANWISE PRESSURE DISTRIBUTION ON WINGS AT 60° ROLL

FIG. 37.

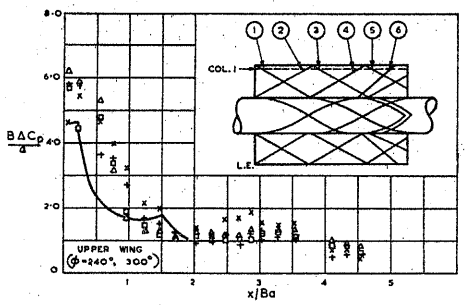

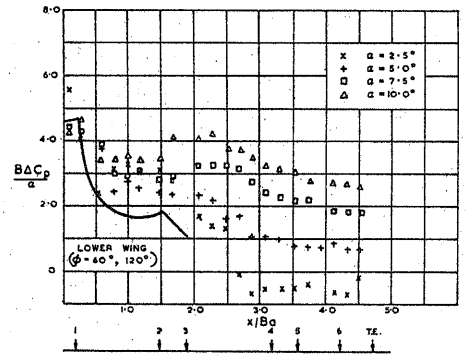

FIG. 38. CHORDWISE DISTRIBUTION OF NORMAL FORCE AT 60° ROLL y/a = 2·49 (Col. 1)

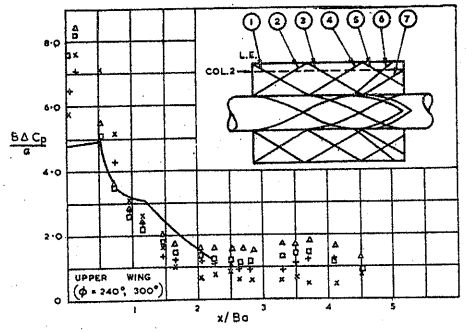

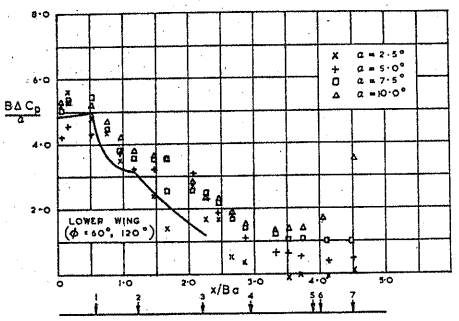

FIG. 39. CHORDWISE DISTRIBUTION OF NORMAL FORCE AT 60° ROLL. y/a = 2·15 (Col. 2)

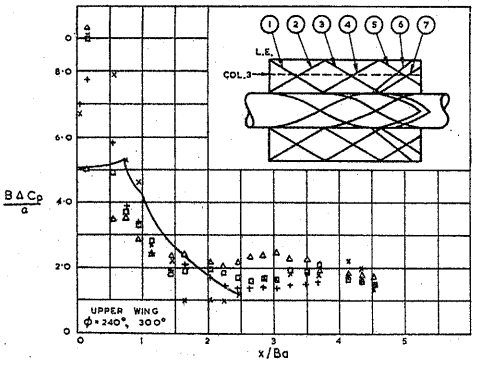

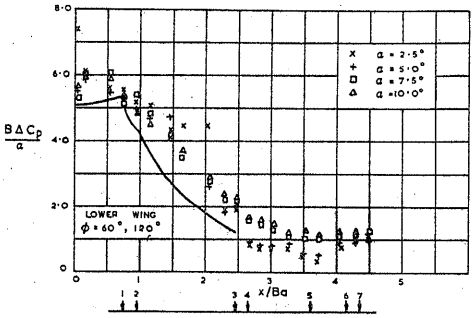

FIG. 40. CHORDWISE DISTRIBUTION OF NORMAL FORCE AT 60° ROLL y/a = 1·94 (Col. 3)

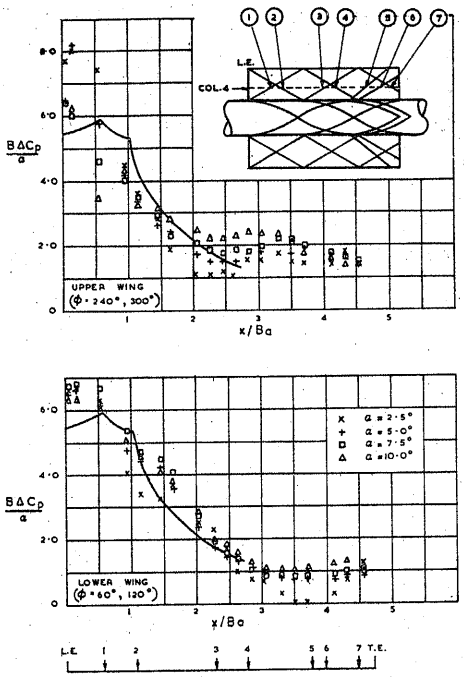

FIG 41. CHORDWISE DISTRIBUTION OF NORMAL FORCE AT 60° ROLL y/a=1·625 (Col. 4)

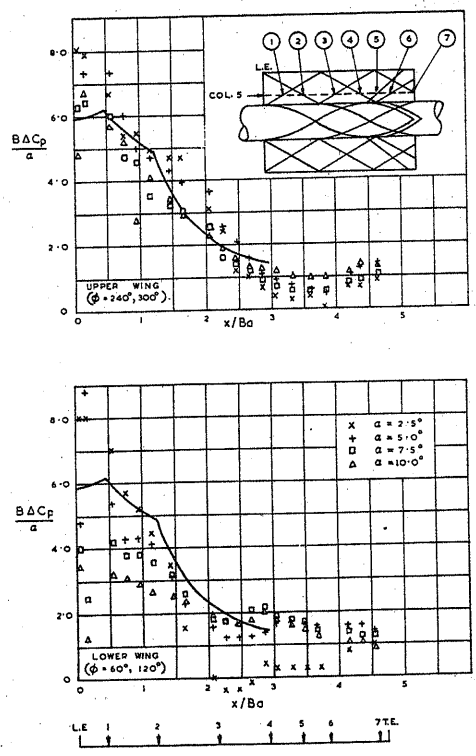

FIG.42. CHORDWISE DISTRIBUTION OF NORMAL FORCE AT 60° ROLL y/a=1·43 (Col. 5)

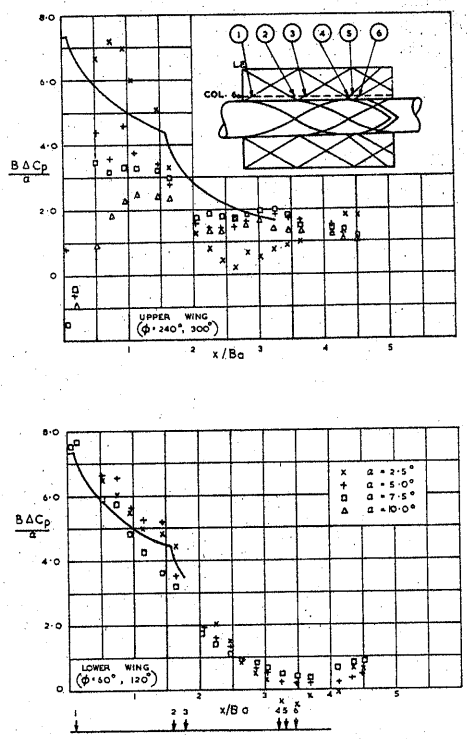

FIG. 43. CHORDWISE DISTRIBUTION OF NORMAL FORCE AT 60° ROLL y/a=1·09 (Col. 6)

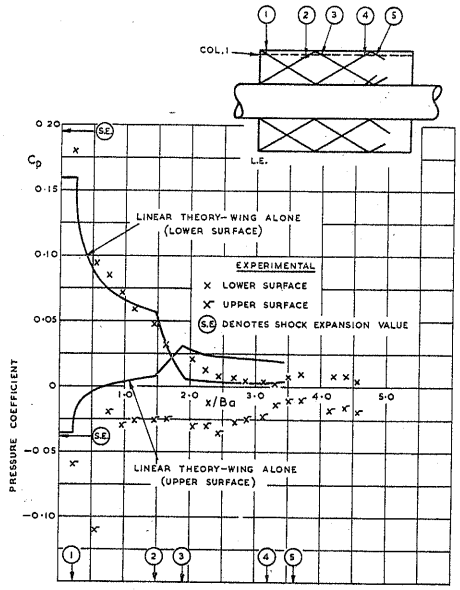

FIG. 44. COMPARISON OF PRESSURE DISTRIBUTION WITH LINEAR THEORY FOR WING ALONE (REFLECTION PLANE AT WING ROOT)
$y/a = 2{\cdot}49 \quad \alpha = 5°$

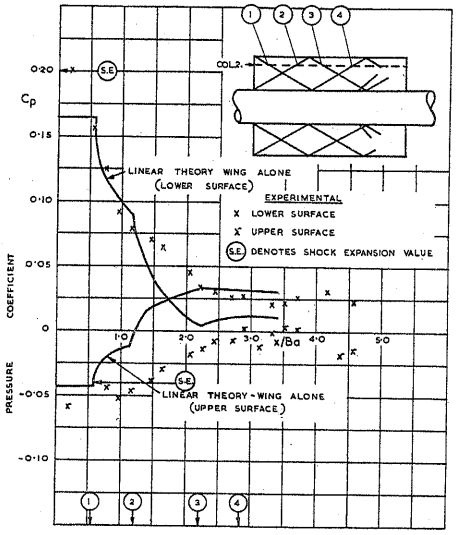

FIG. 45. COMPARISON OF PRESSURE DISTRIBUTION WITH LINEAR THEORY FOR WING ALONE (REFLECTION PLANE AT WING ROOT)
$y/a = 2{\cdot}15 \quad \alpha = 5°$

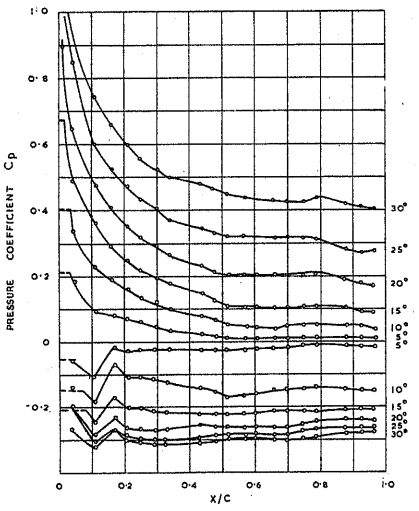

FIG. 46 HIGH INCIDENCE PRESSURE DISTRIBUTION 0° ROLL
y/a = 2·49

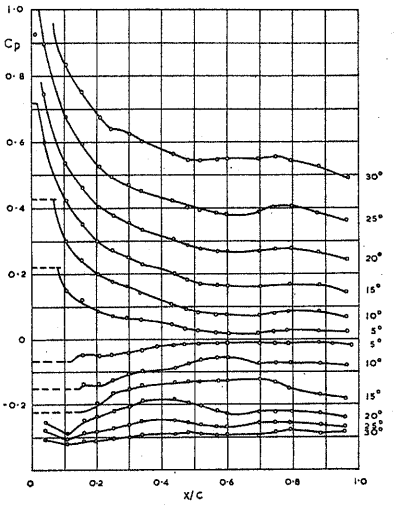

FIG. 47. HIGH INCIDENCE PRESSURE DISTRIBUTION 0° ROLL
y/a = 2·15

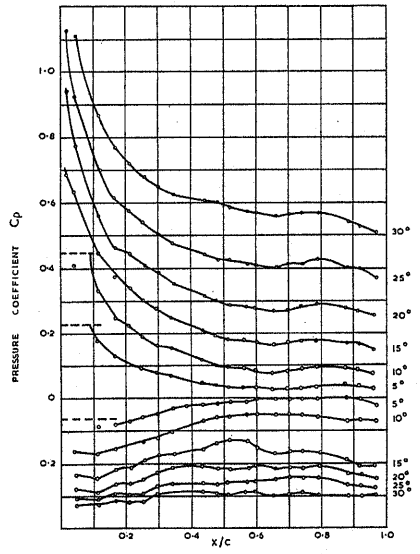

FIG. 48. HIGH INCIDENCE PRESSURE DISTRIBUTION 0° ROLL
y/a = 1·94

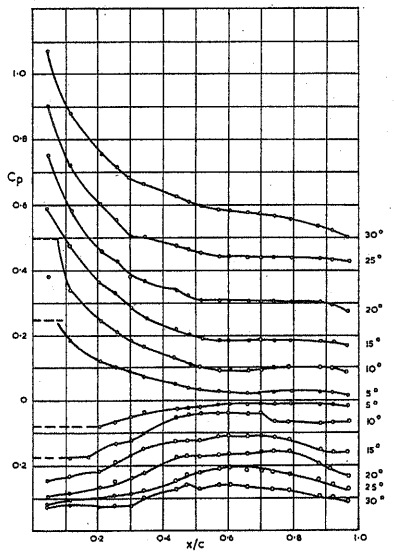

FIG. 49. HIGH INCIDENCE PRESSURE DISTRIBUTION 0° ROLL
y/a = 1·625

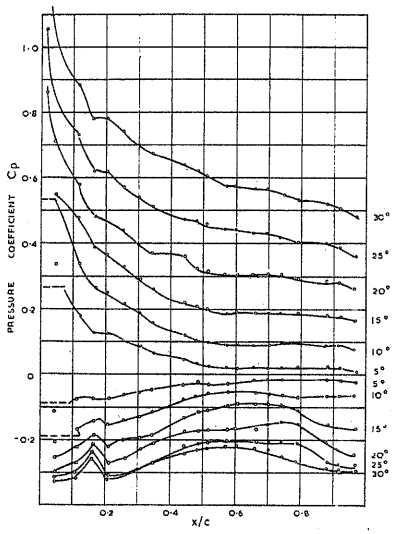

FIG. 50. HIGH INCIDENCE PRESSURE DISTRIBUTION 0° ROLL
y/a = 1·43

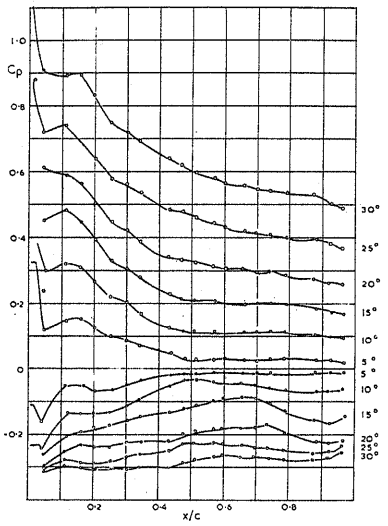

FIG. 51. HIGH INCIDENCE PRESSURE DISTRIBUTION 0° ROLL
y/a = 1·09

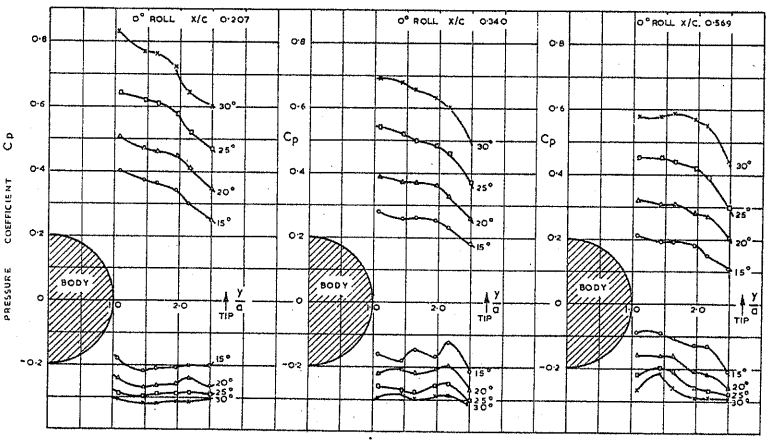

FIG. 52. SPANWISE HIGH INCIDENCE PRESSURE DISTRIBUTION ON WINGS AT 0° ROLL

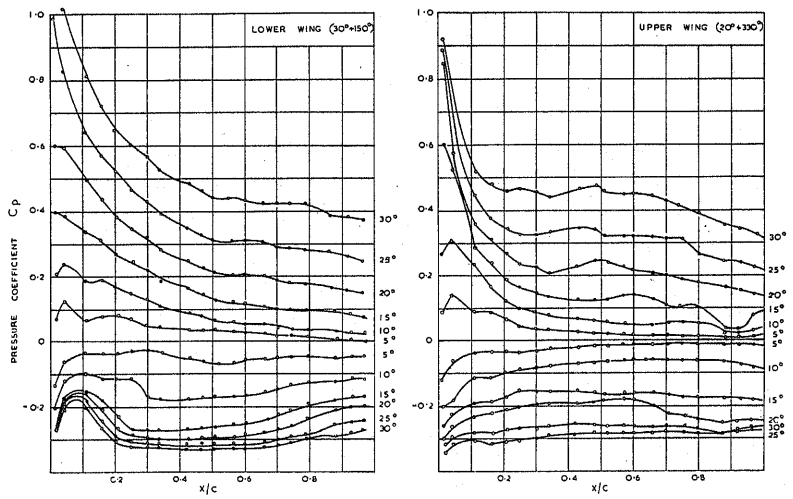

FIG. 53. HIGH INCIDENCE PRESSURE DISTRIBUTION ON WINGS AT 30° ROLL
y/a = 2·49

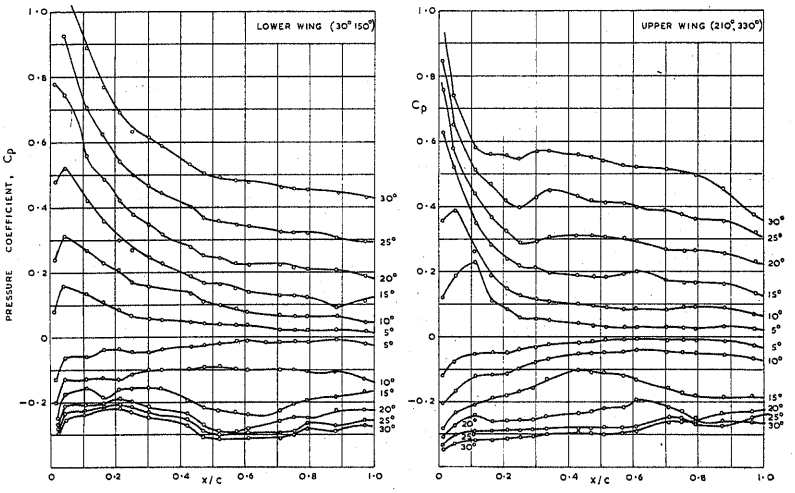

FIG. 54. HIGH INCIDENCE PRESSURE DISTRIBUTION ON WINGS AT 30° ROLL
y/a = 2·15

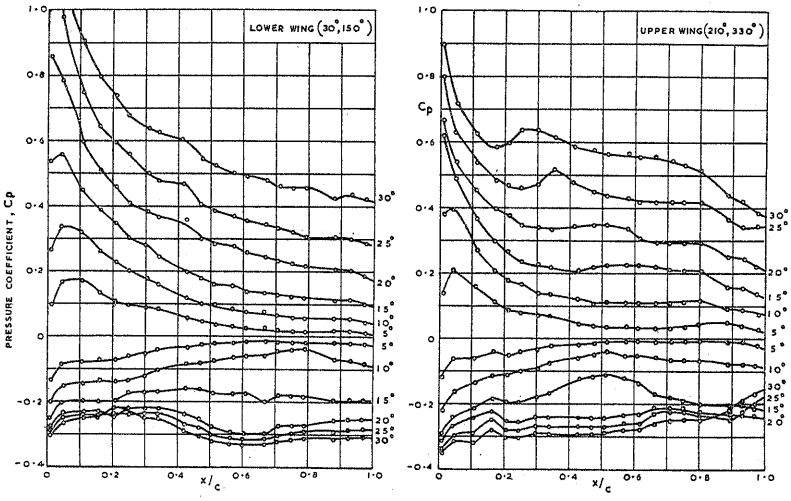

FIG. 55. HIGH INCIDENCE PRESSURE DISTRIBUTION ON WINGS AT 30° ROLL
y/a = 1·94

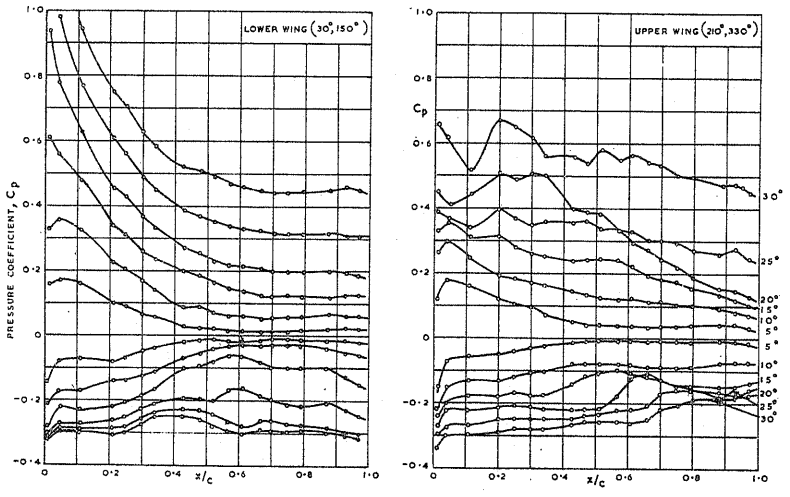

FIG. 56. HIGH INCIDENCE PRESSURE DISTRIBUTION ON WINGS AT 30° ROLL
y/a = 1·625

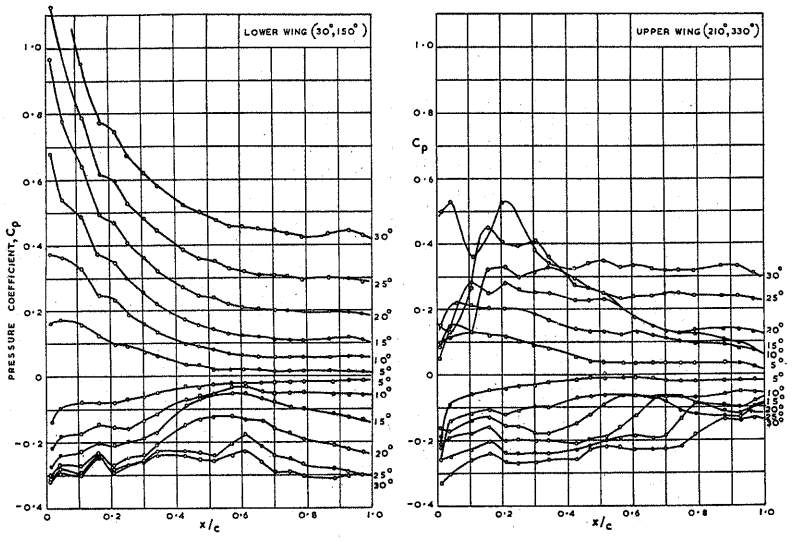

FIG. 57. HIGH INCIDENCE PRESSURE DISTRIBUTION ON WINGS AT 30° ROLL
y/a = 1·43

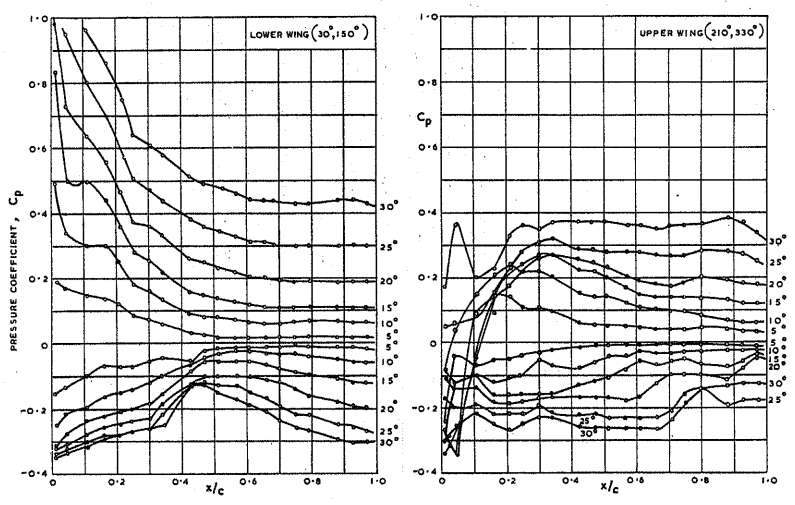

FIG. 58. HIGH INCIDENCE PRESSURE DISTRIBUTION ON WINGS AT 30° ROLL
y/a = 1·09

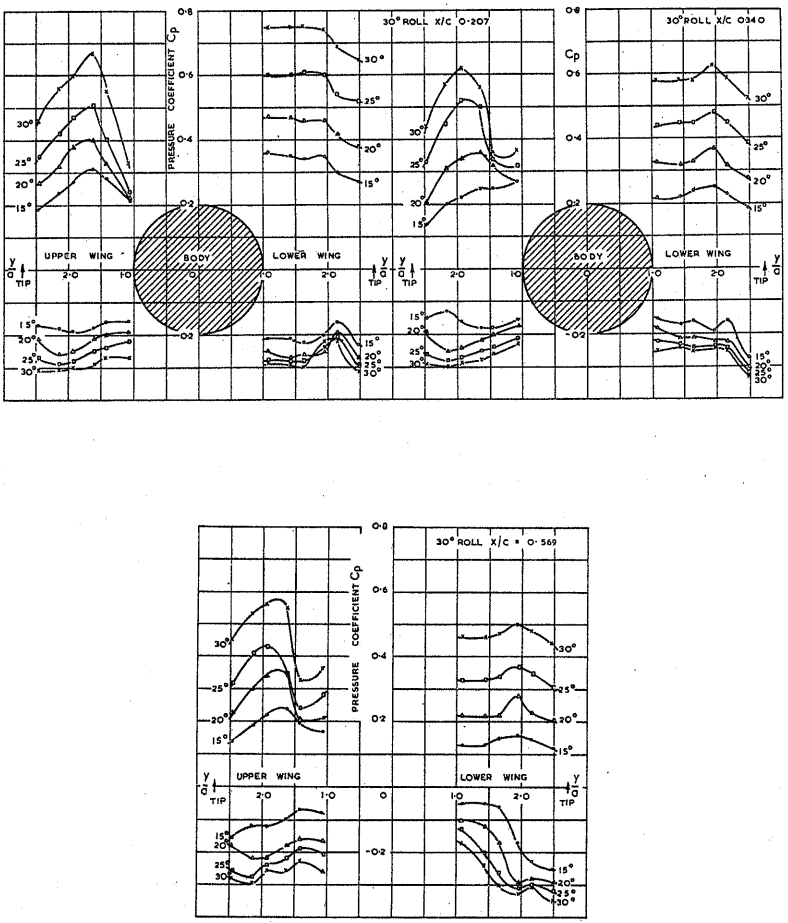

FIG. 59. SPANWISE HIGH INCIDENCE PRESSURE DISTRIBUTION AT 30° ROLL.

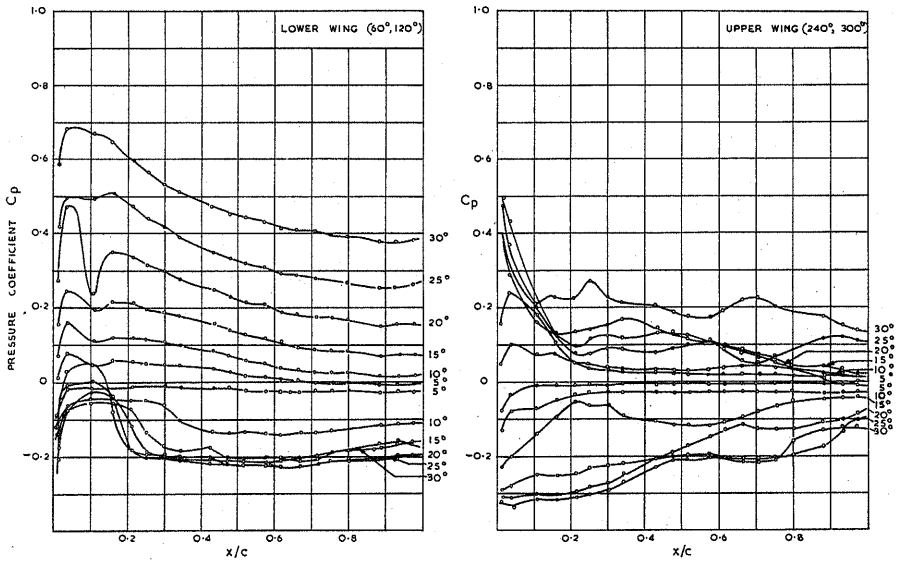

FIG. 60. HIGH INCIDENCE PRESSURE DISTRIBUTION ON WINGS AT 60° ROLL
y/a = 2·49

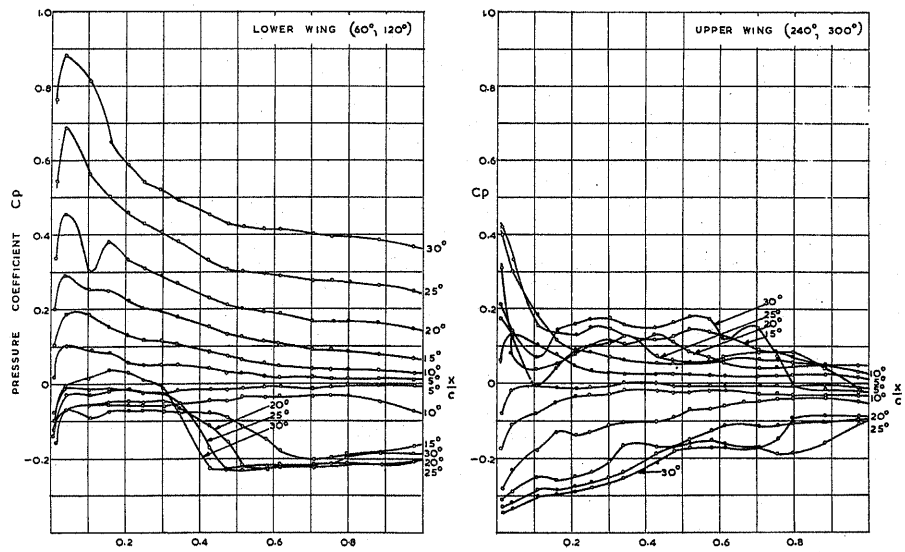

FIG. 61 HIGH INCIDENCE PRESSURE DISTRIBUTION ON WINGS AT 60° ROLL y/a = 2·15

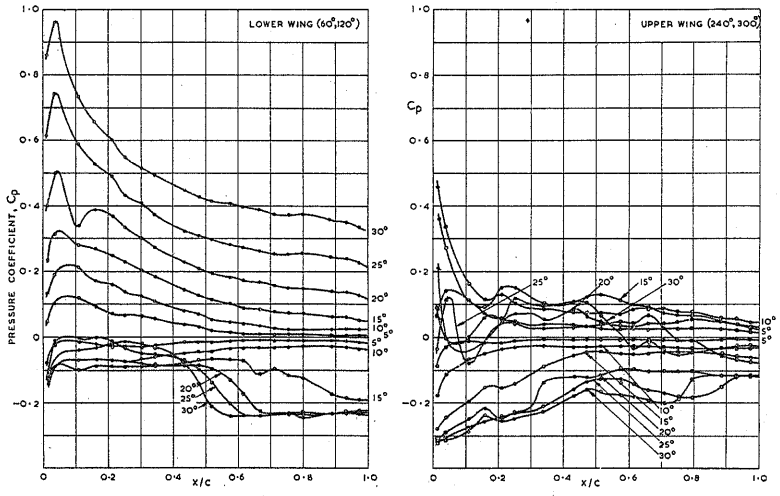

FIG. 62. HIGH INCIDENCE PRESSURE DISTRIBUTION ON WINGS AT 60° ROLL
y/a = 1·94

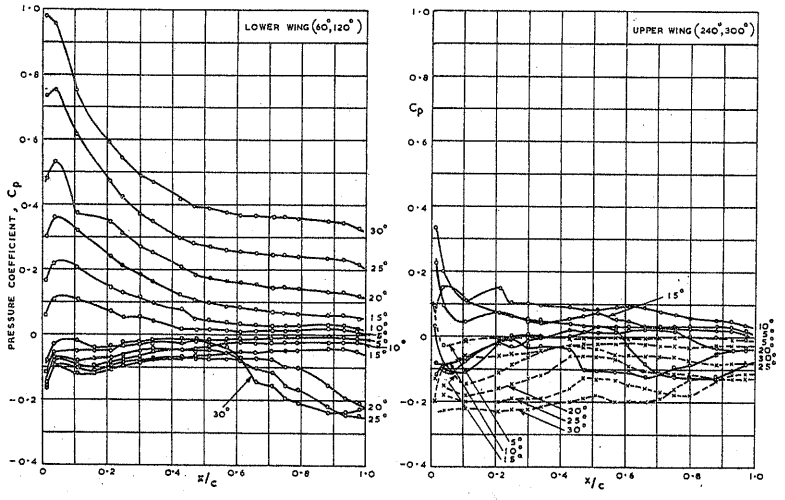

FIG. 63. HIGH INCIDENCE PRESSURE DISTRIBUTION ON WINGS AT 60° ROLL
y/a = 1·625

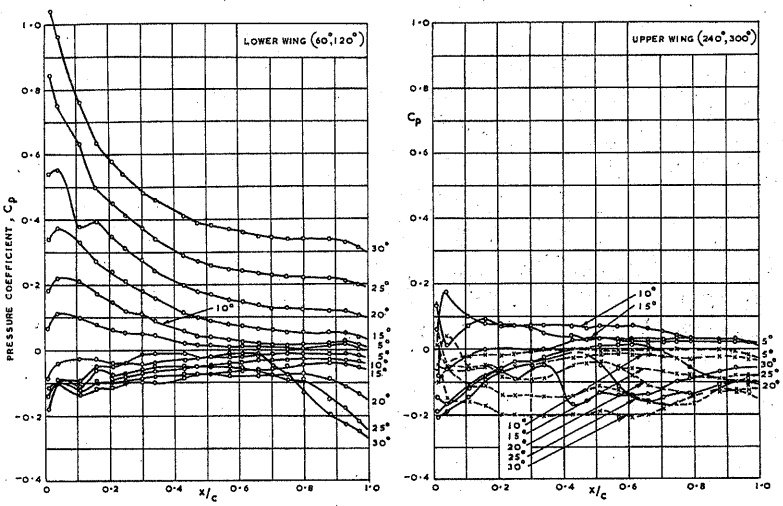

FIG. 64. HIGH INCIDENCE PRESSURE DISTRIBUTION ON WINGS AT 60° ROLL
y/a=1·43

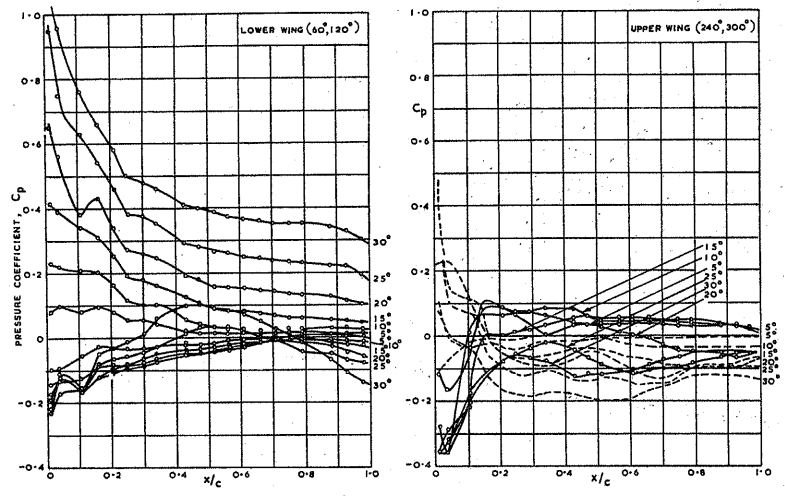

FIG. 65. HIGH INCIDENCE PRESSURE DISTRIBUTION ON WINGS AT 60° ROLL
y/a=1·09

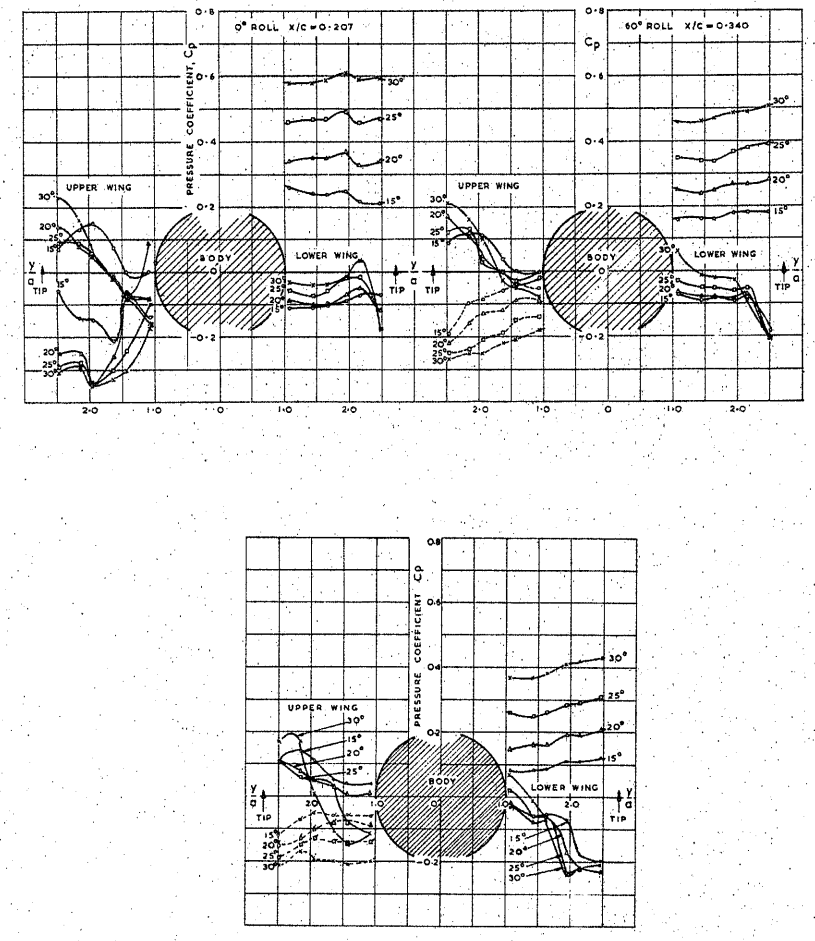

FIG. 66. SPANWISE HIGH INCIDENCE PRESSURE DISTRIBUTION AT 60° ROLL

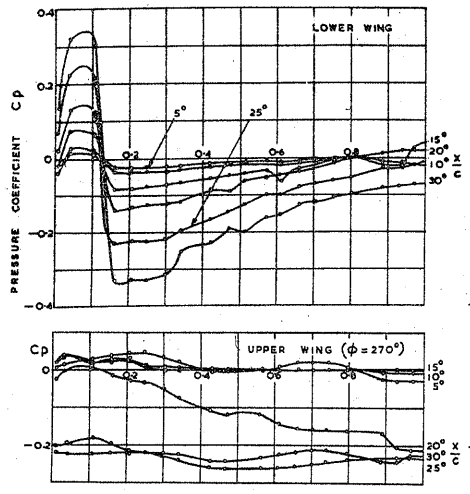

FIG. 67 HIGH INCIDENCE PRESSURE DISTRIBUTION AT 90° ROLL y/a=2·49

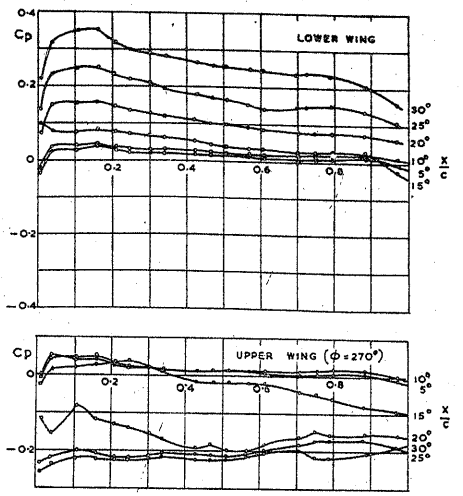

FIG.68 HIGH INCIDENCE PRESSURE DISTRIBUTION AT 90° ROLL y/a=2·15

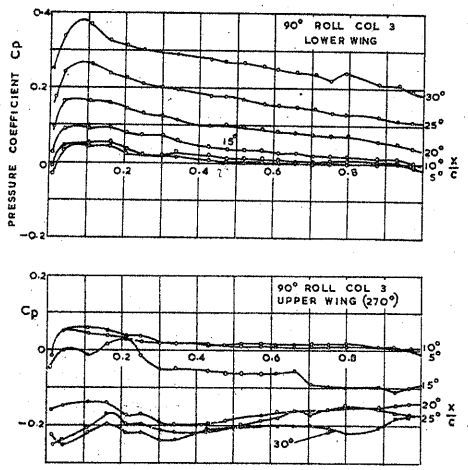

FIG. 69 HIGH INCIDENCE PRESSURE DISTRIBUTION AT 90° ROLL y/a=1·94

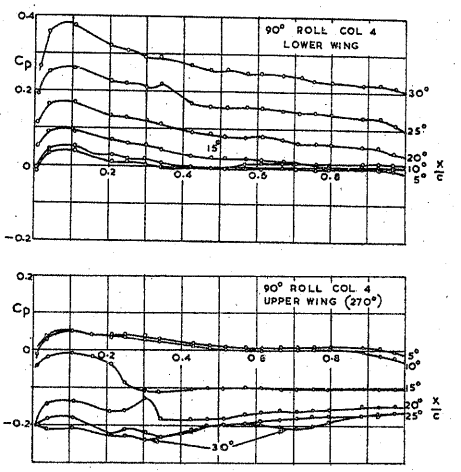

FIG.70 HIGH INCIDENCE PRESSURE DISTRIBUTION AT 90° ROLL y/a=1·625

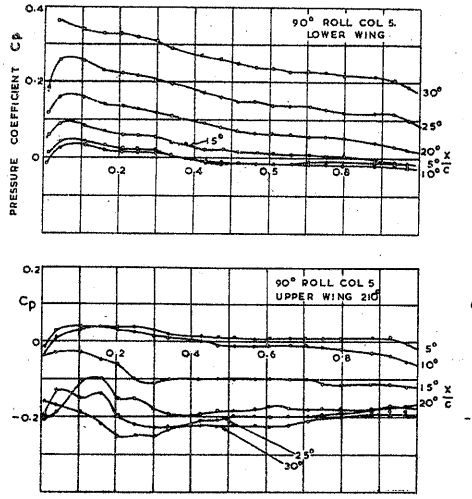

FIG. 71 HIGH INCIDENCE PRESSURE DISTRIBUTION AT 90° ROLL y/a=1·43

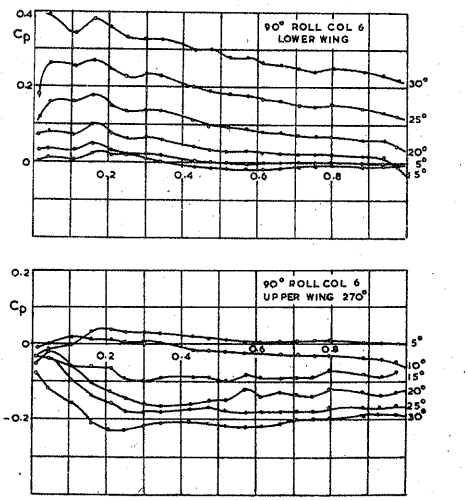

FIG. 72 HIGH INCIDENCE PRESSURE DISTRIBUTION AT 90° ROLL y/a=1·09

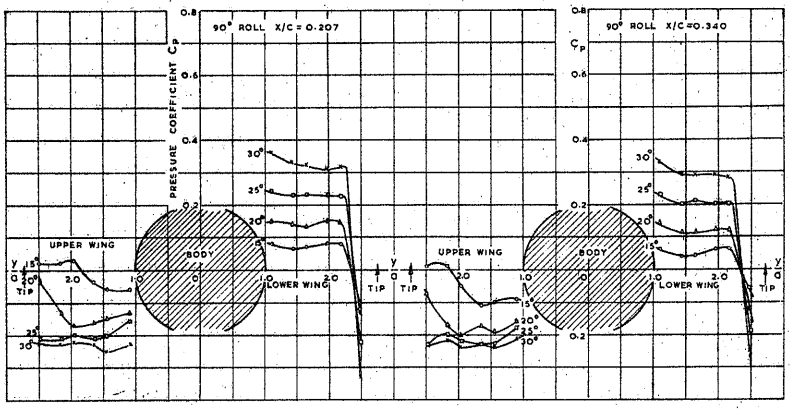

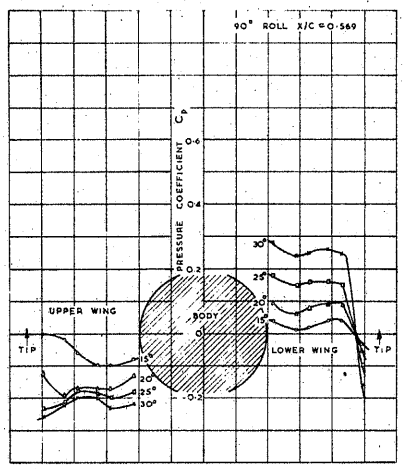

FIG. 73. SPANWISE HIGH INCIDENCE PRESSURE DISTRIBUTION AT 90° ROLL.

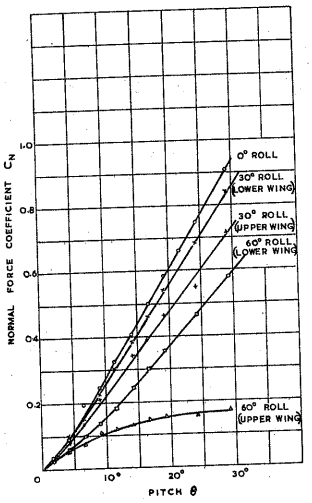

FIG 74. VARIATION OF NORMAL FORCE COEFFICIENT WITH PITCH ANGLE FOR EACH HALF WING

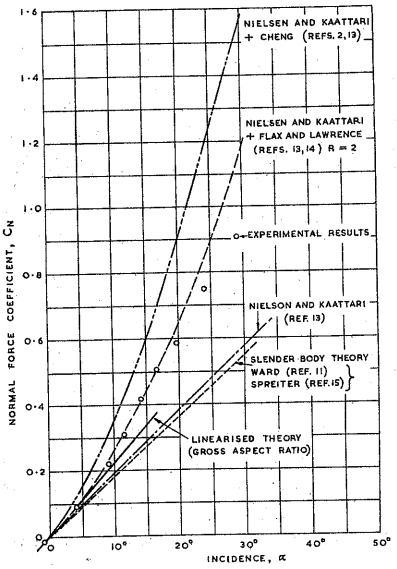

FIG. 75. COMPARISON OF NORMAL FORCE COEFFICIENTS AT ZERO ROLL WITH THEORY

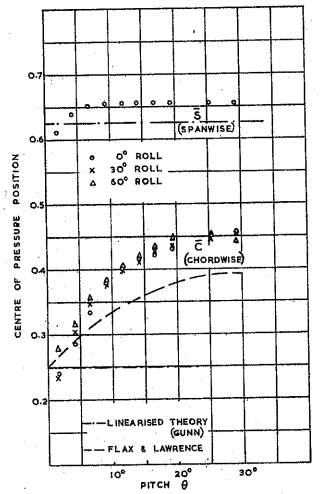

FIG 76 VARIATION OF SPANWISE AND CHORDWISE CO-ORDINATES OF CENTRE OF PRESSURE WITH PITCH ANGLE FOR VARIOUS ROLL ANGLES (BOTH HALF-WINGS IN COMBINATION)

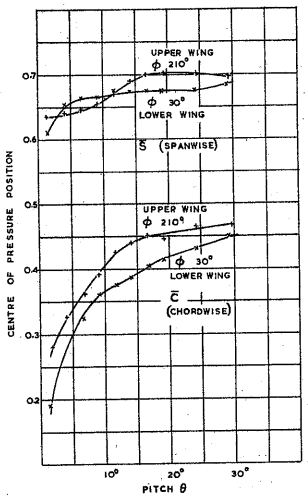

FIG 77 VARIATION OF SPANWISE AND CHORDWISE CO-ORDINATES OF CENTRE OF PRESSURE WITH PITCH ANGLE FOR 30° ROLL

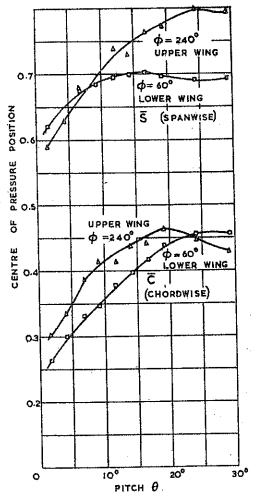

FIG 78. VARIATION OF SPANWISE AND CHORDWISE CO-ORDINATES OF CENTRE OF PRESSURE WITH PITCH ANGLE FOR 60° ROLL

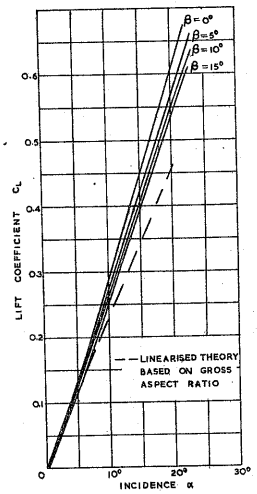

FIG 79. VARIATION OF LIFT COEFFICIENT WITH INCIDENCE

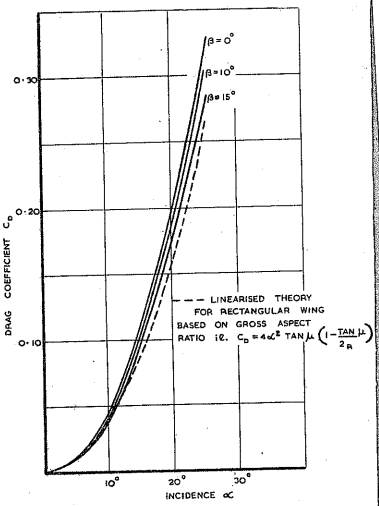

FIG 80. VARIATION OF DRAG COEFFICIENT WITH INCIDENCE

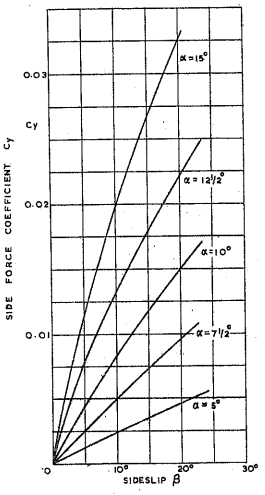

FIG 81 VARIATION OF SIDE-FORCE COEFFICIENT WITH ANGLE OF SIDESLIP

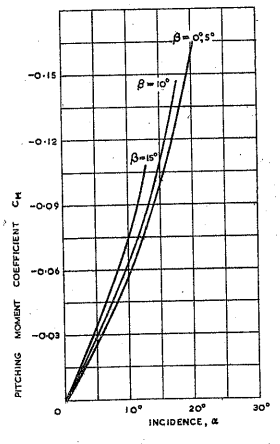

FIG. 82. VARIATION OF PITCHING MOMENT COEFFICIENT WITH ANGLE OF INCIDENCE (ABOUT 1/4 CHORD POINT)

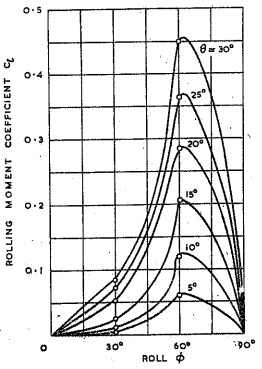

FIG. 83. VARIATION OF ROLLING MOMENT COEFFICIENT WITH ROLL ANGLE